PERGAMON

International Journal of Solids and Structures 38 (2001) 6455–6489

INTERNATIONAL JOURNAL OF SOLIDS and STRUCTURES

www.elsevier.com/locate/ijsolstr

Normal and tangential force–displacement relations for frictional elasto-plastic contact of spheres

Loc Vu-Quoc *, Xiang Zhang [1], Lee Lesburg [2]

Department of Aerospace Engineering, Mechanics and Engineering Science, University of Florida, 231 Aerospace Engineering Building, P.O. Box 116250, Gainesville, FL 32611-6250, USA

Received 22 May 2000; in revised form 6 March 2001

Abstract

In this paper, we present the data obtained from numerical experiments that are at the foundation of our successful elasto-plastic force–displacement (FD) models in both the normal direction and tangential direction of spheres in collision. We also present in detail how these data were obtained. Our numerical experiments are in the form of frictional elasto-plastic finite-element analysis of spherical particles in contact. We use the numerical experiments to observe the behavior of various quantities involved in the contact (e.g. contact-area radius, contact curvature, stresses, FD relations, etc.). This observation has helped us to devise an accurate and consistent model for frictional elasto-plastic contact of spherical particles that are used in granular-flow simulations that may involve tens of thousands of these particles.

Keywords: Spheres; Elasto-plastic contact; Force–displacement relations

1. Introduction

A growing number of agricultural and industrial processes involve particulate systems. These systems pose significant challenges to the gathering of engineering data and to the design of handling equipment. The chute flow of soybeans, for example, is difficult to study quantitatively given that most measurement methods cause irrevocable changes to the flow. Nonintrusive experimental methods are available, but equipment cost is often prohibitive. Computer simulation of such systems is a viable alternative.

The discrete element method (DEM) is a numerical simulation technique that can be used to investigate the flow properties of granular materials. For a pair of particles in contact, the DEM employs force–displacement (FD) models to calculate the resulting contact forces acting on the particles. The FD model provides contact force as a function of relative displacement or *overlap* between the particles. Most

* Corresponding author. Tel.: +1-352-392-6227; fax: +1-352-392-7303.
E-mail address: vu-quoc@ufl.edu (L. Vu-Quoc).
URL: http://www.aero.ufl.edu/~vql.
[1] Now with Siemens Corp., Princeton, NJ.
[2] Now with PTC, Needham, MA.

0020-7683/01/$ - see front matter
PII: S0020-7683(01)00065-8

simulation algorithms apply this function incrementally, with increments in displacement giving rise to increments in contact force. All contact forces and moments acting on a particle are then used as input to solve the equations governing the rigid-body motion of that particle. The solution of these equations of motion will lead to new displacement increments, and the computational procedure repeats itself with the computation of new increments of contact forces. The readers are referred to Vu-Quoc et al. (2000c) for a detailed exposition of the DEM for the flow of elliptical particles.

In most granular flow regimes, it is unrealistic to assume that contact deformations remain in the elastic range of material response, even though energy is dissipated through friction, since the coefficient of restitution at impact is in general less than one, due to the plastic deformation that occurs near the contact point. Energy dissipation resulting from plastic deformation is important and must be modeled. Ad hoc use of dampers whose coefficients must be obtained through trial and error was often employed (e.g., Thornton and Randall, 1988; Mishra, 1995). In our research program, we propose to develop an FD model that accounts for frictional elasto-plastic response based on well-founded fundamental contact mechanics theory.

Despite the need to account for plastic deformation, elastic contact mechanics provides the foundation for existing FD models. Hertz (1882) presented the normal FD (NFD) relation for spheres in contact and subjected to a normal force. Using Hertz theory, Cattaneo (1938a,b,c) and Mindlin (1949) independently derived the tangential FD (TFD) relation for identical elastic spheres in elastic-frictional contact, subjected to a constant normal force and a varying tangential force. By far the most complex of the contact theories is the one presented in Mindlin and Deresiewicz (1953), which provided an incremental TFD relation for identical elastic spheres subjected to varying normal and tangential forces. For brevity, we refer to the collection of these elastic frictional contact mechanics theories – i.e., Hertz, Cattaneo, Mindlin, and Deresiewicz – together as the HCMD theory.

Some publications have presented partial validations of the components of the HCMD theory. Johnson (1985) summarized results from experiments that reproduced key phenomena (e.g., micro-slip, energy loss, attrition) of the theory's tangential component. Shih et al. (1992) presented an experimental and FEA validation of the stress distributions of Hertz theory, but no verification of the NFD relation. To the best of our knowledge, a validation of the elastic-frictional TFD relation by FEA has not been widely known in the literature. However, some publications have addressed similar effects in frictional contact studies (e.g., Chandrasekaran et al., 1987; Cuttino and Dow, 1997).

The effects of plastic deformation on FD relations have been studied only in the normal direction. Johnson (1985) reviewed approximation formulas for the indentation of half-spaces of elasto-plastic material by various rigid indenters. None of these formulas apply to the contact of two elasto-plastic solids. In addition, these formulas do not approximate the loading-unloading relation, which is important for granular flow simulations.

FD studies via elasto-plastic FEA also only addressed the normal direction. Walton (1993) determined by FEA the NFD relation for elasto-plastic spheres in contact and subjected to increasing and decreasing normal loads. Kral et al. (1993), Hardy et al. (1971), and Sinclair et al. (1985) each used FEA to characterize the behavior of an elasto-plastic half-space indented by a rigid sphere. Kral et al. (1995a,b) performed a similar investigation for the indentation of an elasto-plastic layered medium. There have been no published studies on plastic deformation effects in TFD relations.

Some authors have addressed the coefficient of restitution as a measure of the effects of energy dissipation during impact. Brilliantov et al. (1996) employed *viscoelasticity* as the energy dissipation mechanism to calculate the coefficients of restitution for the normal and tangential directions of colliding particles as functions of the impact velocity. Thornton (1997) employed *elasto-plasticity* as the energy dissipation mechanism in his NFD model, which was consistent with the work of Davies (1949) (see also Bitter, 1963; Johnson, 1985). None of the above references had a validation, experimentally or numerically.

By contrast, we have developed an accurate and simple frictional elasto-plastic NFD model (Vu-Quoc and Zhang, 1999; Vu-Quoc et al., 2000b) and TFD model (Vu-Quoc et al., 2000a), all based on the FEA

results presented in this paper. While the FD model is presented in other papers, we do provide in this paper a few basic ideas at the foundation of our elasto-plastic FD model.

2. Normal FD relation

2.1. Hertz theory of normal contact

Hertz considered the normal contact of two spheres i and j, as shown in Fig. 1. (We review Hertz's key results in this section. For a more complete review, see Johnson, 1985.) For sphere i, we consider R_i to be the radius, v_i the Poisson's ratio, and E_i the Young's modulus. Similarly, R_j, v_j, E_j are the properties of sphere j. We (as well as other authors) define for the contact the equivalent elastic modulus E^* and the equivalent contact curvature $1/R^*$ as

$$\frac{1}{E^*} := \left(\frac{1-v_i^2}{E_i} + \frac{1-v_j^2}{E_j} \right), \tag{2.1}$$

and

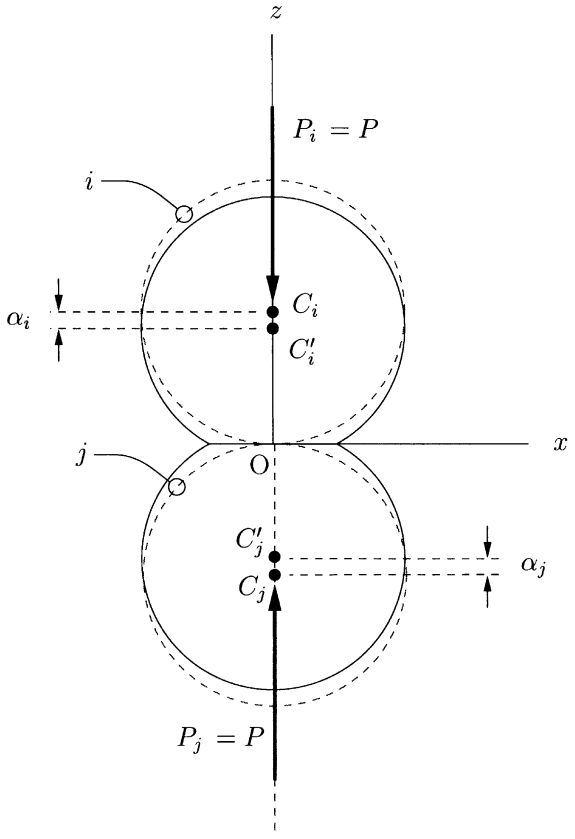

Fig. 1. Two spheres in normal contact.

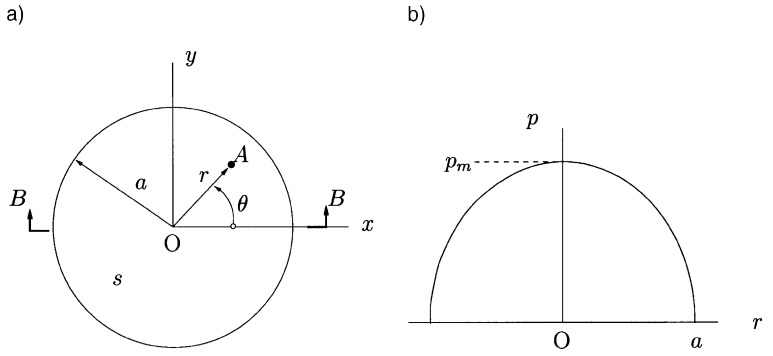

Fig. 2. Contact area and Hertz pressure. (a) Circular contact-area (viewed from $+z$). Section B–B is a contact-area diameter. (b) Hertz normal pressure at section B–B.

$$\frac{1}{R^*} := \left(\frac{1}{R_i} + \frac{1}{R_j}\right). \tag{2.2}$$

Due to axisymmetry, the contact surface s between the spheres is circular with radius a (see Fig. 2(a)). Hertz proposed that the normal pressure on this contact-area is half-elliptical in shape and independent of the angular coordinate θ. That is, at a point A in the contact-area, at a distance r from the center O, the normal pressure $p(r)$ is given by

$$p(r) = p_{\mathrm{m}}\left[1 - \left(\frac{r}{a}\right)^2\right]^{1/2}, \tag{2.3}$$

where p_{m} is the maximum normal pressure occurring at $r = 0$. By integrating p over s and rearranging to solve for p_{m}, we obtain

$$p_{\mathrm{m}} = \frac{3P}{2\pi a^2}. \tag{2.4}$$

Fig. 2(b) shows the Hertz pressure distribution $p(r)$ at a cross-section that is perpendicular to s and through its diameter.

From considerations of surface displacements and contact boundary conditions, Hertz determined that the contact-area radius is related to the normal force by

$$a = \left(\frac{3PR^*}{4E^*}\right)^{1/3}. \tag{2.5}$$

From the same considerations, Hertz found the mutual approach α_{ij} of distant points in the spheres, given by

$$\alpha_{ij} = \alpha_i + \alpha_j = \frac{a^2}{R^*} \tag{2.6}$$

(see also Johnson, 1985). Substituting Eq. (2.5) into Eq. (2.6), we obtain the Hertz (i.e., elastic) version of the NFD relation for contacting spheres, expressed as

$$\alpha_{ij} = \left(\frac{9P^2}{16R^*(E^*)^2}\right)^{1/3} \tag{2.7}$$

Combining Eq. (2.5) with Eq. (2.4), we obtain

$$p_{\mathrm{m}} = \left(\frac{6P(E^*)^2}{\pi^3 (R^*)^2} \right)^{1/3}, \tag{2.8}$$

which provides the maximum contact pressure as a function of the input normal load and the spheres' properties.

By combining expressions from Hertz theory with those of the von Mises yield criterion, one can determine P_{Y}, the normal force that causes incipient yield in spheres in contact. We refer the reader to Vu-Quoc et al. (2000b) for this derivation, but we provide the formula below:

$$P_{\mathrm{Y}} = (1.61)^3 \frac{\pi^3 R^2 (1-\nu^2)^2}{6E^2} \sigma_{\mathrm{Y}}^3, \quad \nu = 0.3. \tag{2.9}$$

(A similar equation appears in Johnson (1985, p. 155, Eqs. (6.9) and (6.10)), but that version was derived using the Tresca yield criterion.)

2.2. Finite element model for normal contact

Fig. 3 shows the domain of analysis for the normal contact of identical spheres of radii $R = 0.1$ m. We apply a symmetric boundary condition along the z-axis and clamp the sphere's equator. We apply the normal load P to the rigid surface and constrain the rigid surface to move in only the z-direction. (Note that although the domain is composed of a sphere and a planar surface, the *deformable* sphere and the *rigid* plane distinguish the domain from those of Kral et al. (1993) and other authors who have modeled rigid indenters contacting deformable half-spaces.)

Fig. 4 shows the FE discretization of the current domain of analysis. The FE mesh of the sphere contains 2204 quadratic axisymmetric triangular elements with ABAQUS designation `CAX6`. Each element has six

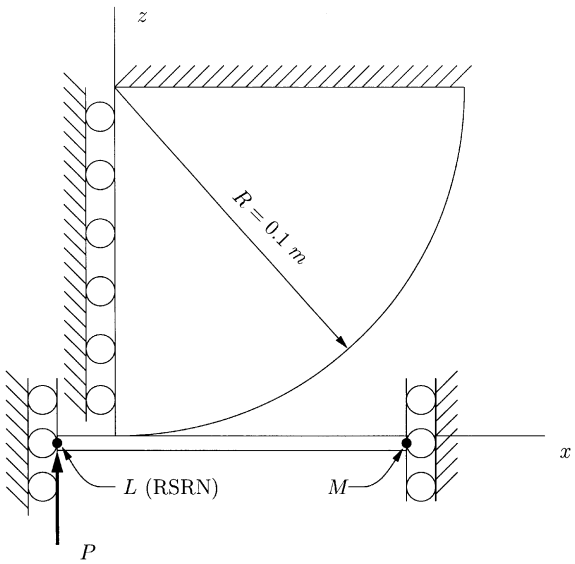

Fig. 3. Domain of analysis for normal contact of identical spheres.

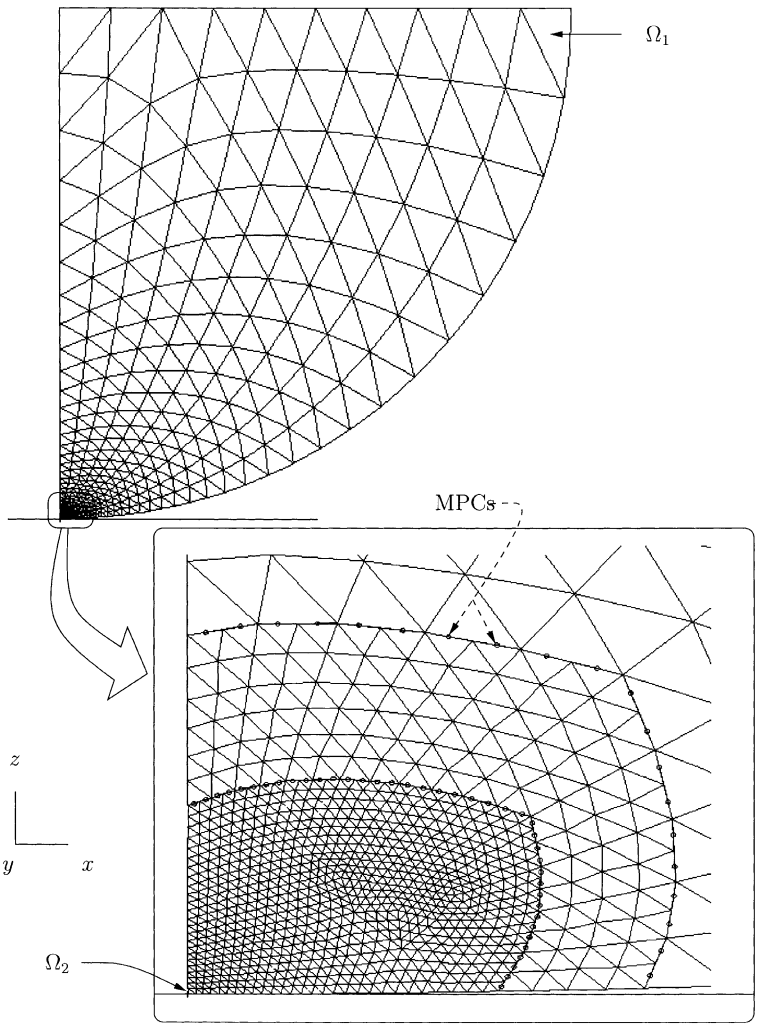

Fig. 4. Axisymmetric FE mesh for normal contact of identical spheres. High degree of mesh refinement near contact. Multiple point constraints (MPCs).

integration points – three at the vertices and three on the element edges. To accomplish the degree of mesh refinement that is shown in Fig. 4, we recursively split the triangular elements and impose quadratic multipoint constraints (MPCs) on the nodes that lie on the interface between relatively coarse and relatively refined mesh regions. In Fig. 4, circular markers designate nodes whose displacements are constrained by MPCs.

As an indication of the degree of mesh refinement that is in Fig. 4, we compare the average edge lengths of two elements within the FE mesh. Far from the contact-area, element Ω_1 has an average edge length of $\overline{h}_1 = 1.59 \times 10^{-2}$ m $\approx R/6$. Near the contact, however, element Ω_2 has an average edge length of $\overline{h}_2 = 4.36 \times 10^{-5}$ m $\approx R/2300$. (Note that we compare edge lengths because the edge length of Ω_2 has important implications for the determination of the FE contact-area radius a_{FE}. see Section 2.3.)

The rigid surface in Fig. 4 is a rigid surface segment that extends from $L(-0.01, 0, 0)$ to $M(0.05, 0, 0)$. We take the node at L to be the rigid surface reference node (RSRN) and apply all loads to this node. To obtain

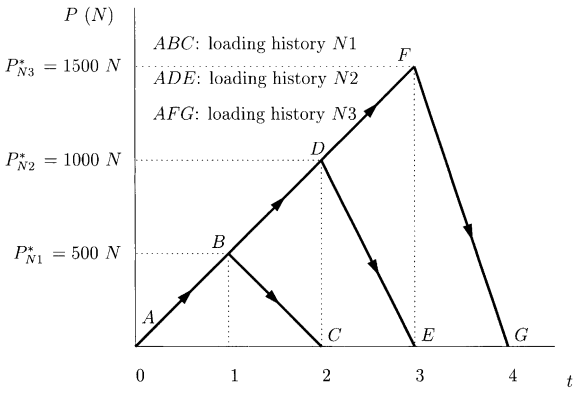

Fig. 5. Normal loading histories.

FD relationships from the FEA, we track through time the applied normal force and the z-displacement of the RSRN.

To impose contact constraints, we incorporate four-node rigid surface interface elements with ABAQUS designation `IRS22A`. Each of these elements shares three nodes with a `CAX6` element on the sphere's surface. The RSRN is the fourth node of all of the interface elements.

Fig. 5 shows the loading histories that we apply in this study of normal loading. While the loading rates are uniform among the loading histories, the unloading rates vary. In fact, the loading and unloading rates are irrelevant to the problem due to Remark 2.1.

Remark 2.1. We treat the contact of the spheres as a static problem in the FE solution procedure. In addition, we use *time-independent* plasticity as a material property. The applicability of static FE solutions to the (dynamic) impact of spheres is ensured by the comparison of the impact velocity with the stress wave velocity in the spheres' material. As proposed in Johnson (1985), a *quasistatic* condition is achieved for two impacting spheres when

$$0.3\left(\frac{v}{w}\right)^{3/5} \ll 1, \tag{2.10}$$

where v is the impact velocity and w the wave velocity. For a thorough discussion of stress waves see Goldsmith (1960). ■

For the sphere of radius $R = 0.1$ m, we choose the material properties of the aluminum alloy Al 1100-H14 (99% Al): Young's modulus $E = 7.0 \times 10^{10}$ N/m^2, Poisson's ratio $\nu = 0.3$, and yield stress $\sigma_Y = 1.0 \times 10^8$ N/m^2. Using Eq. (2.9), we find the normal force at incipient yield $P_Y = 36.4$ N for these sphere properties. (Note, then, that loading history $N3$ reaches a maximum normal force that is approximately 41 times larger than P_Y. We expect significant plastic flow in the case of loading history $N3$.) Note that the choice of these geometry and material properties is only for the numerical experiments. The results are valid in general.

In our FEA involving elasto-plastic material properties, we apply the von Mises yield criterion. According to the von Mises criterion, yielding occurs when

$$f = J_2 - k^2 = 0, \tag{2.11}$$

where k is a material property and J_2 the second invariant of the deviatoric stress tensor $\boldsymbol{S}$, given by

$$J_2 = \tfrac{1}{2} S_{ij} S_{ij}, \tag{2.12}$$

where

$$S_{ij} = \sigma_{ij} - \tfrac{1}{3}\delta_{ij}\sigma_{kk}. \tag{2.13}$$

For *perfect* plasticity of the sphere material that we adopt in this study, the constant k is simply

$$k = \frac{\sigma_{\mathrm{Y}}}{\sqrt{3}}, \tag{2.14}$$

where σ_{Y} is the material's yield stress under uniaxial tension. By substituting Eqs. (2.12) and (2.14) into Eq. (2.11), we express the yield criterion in the simpler form

$$\sigma_{\mathrm{vM}} = \left[\frac{3}{2} S_{ij} S_{ij}\right]^{1/2} = \sigma_{\mathrm{Y}}, \tag{2.15}$$

where σ_{vM} is the von Mises equivalent stress.

Remark 2.2. Although perfect plasticity was used to model the material response, there is a "shell" around the plastic zone, that can take additional load. Thus when we look at the behavior of the contact-area radius, observe a response that is similar to plasticity with hardening. ■

2.3. FEA calibration

To calibrate the FE model of Fig. 4 we apply loading history $N3$ to a sphere with the elastic material properties that are listed in Section 2.2. That is, we perform model verification without considering the von Mises yield condition. We compare FE results (indicated by subscript FE) with quantities that are given by Hertz theory (indicated by subscript H).

Fig. 6 shows for the elastic verification the normal force P plotted against the normal displacement α_{FE}. Recall that α_{FE} is the z-direction displacement of the RSRN. The P versus α_{FE} relation follows closely the Hertzian relation (2.7). At the maximum normal force $P_3^* = 1500$ N, the displacement α_{FE} differs from the prediction α_{H} by only 0.37%. Note that the loading and the unloading curves both follow the same path in

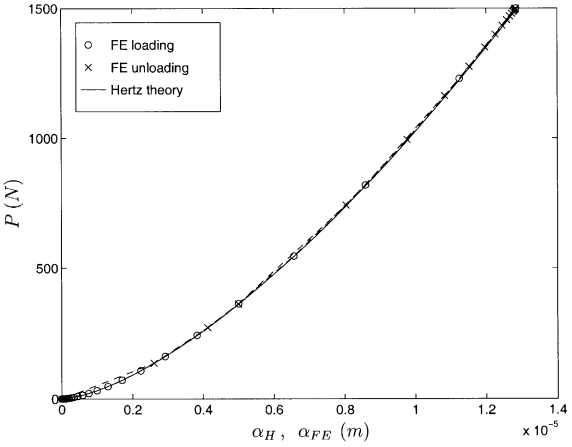

Fig. 6. Normal force P versus normal displacement α_{FE} for axisymmetric elastic verification. Loading history $N3$. Hertzian expression given by Eq. (2.7).

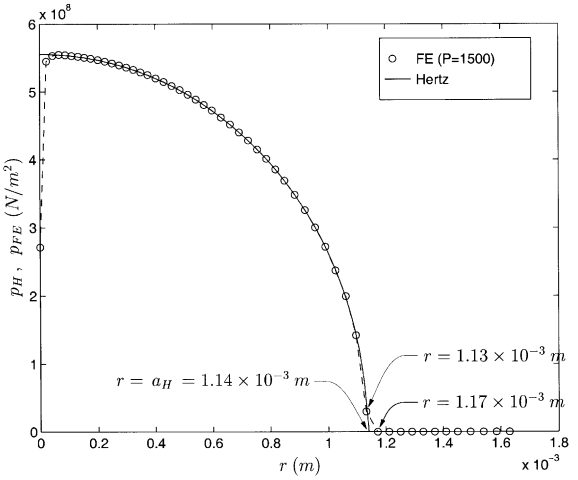

Fig. 7. Normal pressure p_{FE} exerted on IRS22A elements for the elastic verification. Hertzian expression for p_{H} given by Eq. (2.3). FE contact-area radius: $1.13 \times 10^{-3} < a_{\mathrm{FE}} < 1.17 \times 10^{-3}$ m.

the (P, α) space. This behavior is explained by the fact that we apply only elastic material properties and also the fact that we use a frictionless rigid surface. There is no energy loss due to either plastic flow or friction.

Fig. 7 shows at $P_3^* = 1500$ N the normal pressure p_{FE} that is exerted on the IRS22A elements at the sphere-rigid surface interface. The small edge lengths of the IRS22A elements result in a close approximation of the Hertz pressure p_{H}. The contact pressure for the data point at $r = 0$ is considerably lower than that for the remaining data points. We attribute the difference to either (i) numerical errors, or (ii) incorrect stress interpolation due to the missing adjacent (mirror image) element.

While the FE contact-area radius a_{FE} is not directly available as an output variable from ABAQUS, Fig. 7 implies that it is possible to determine a range of values for the location of the edge of the contact-area. Recall that the contact-area radius is defined as the value of the radius r at which the normal pressure goes to zero. In Fig. 7, we know only discrete values of normal pressure, but we surmise that, starting from the node on the z-axis, a_{FE} must lie between the last node in contact and the first node that is not in contact. For the data points that are shown in Fig. 7, a_{FE} lies in the range $1.13 \times 10^{-3} \leqslant a_{\mathrm{FE}} \leqslant 1.17 \times 10^{-3}$ m.

To obtain a specific value for a_{FE}, we choose the outermost or larger value of the range limits. That is, for $P_3^* = 1500$ N, the elastic verification predicts a contact-area radius of $a_{\mathrm{FE}} = 1.17 \times 10^{-3}$ m. This value of a_{FE} is 3.0% greater than the Hertzian value $a_{\mathrm{H}} = 1.14 \times 10^{-3}$ m given by Eq. (2.5) from Hertz theory.

For simplicity, we use the name *node-distance* to describe the above method for determining a_{FE}. In summary, the node-distance method interprets the FE contact-area radius a_{FE} as the radial position of the first node that is not in contact with the rigid surface. Note that, as shown in Fig. 7, the choice of this node inherently causes *overestimation* in the computed contact-area radius a_{FE}.

In Fig. 8 we plot the variation of a_{FE} with the normal force P, where each value of a_{FE} is determined via the node-distance method. While the FE data in Fig. 8 does follow closely the Hertzian relationship in Eq. (2.5), the FE curve does show the overestimation of a_{FE} due to the use of the node-distance method. That is, $a_{\mathrm{FE}} > a_{\mathrm{H}}$ for most values of P. A better estimation of a_{FE} could be employed, i.e., by averaging or by polynomial extrapolation.

For the elastic verification, Fig. 9 shows the error $a_{\mathrm{err}} := a_{\mathrm{FE}} - a_{\mathrm{H}}$ for both loading and unloading. In addition, Table 1 lists the values of the maximum, minimum, and mean a_{err} for the loading and unloading. Note that, as percentages of the maximum $a_{\mathrm{H}} = 1.14 \times 10^{-3}$ m, the mean errors are small: 1.60% for

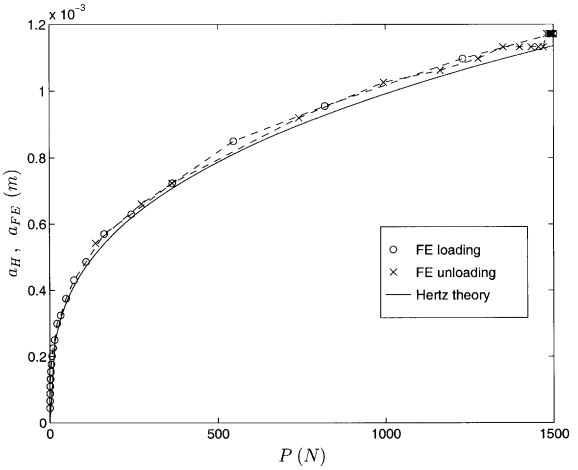

Fig. 8. Computed contact-area radius a_{FE} versus normal force P for elastic verification. Hertzian expression for a_{H} given by Eq. (2.5). *Node-distance* method to determine a_{FE}.

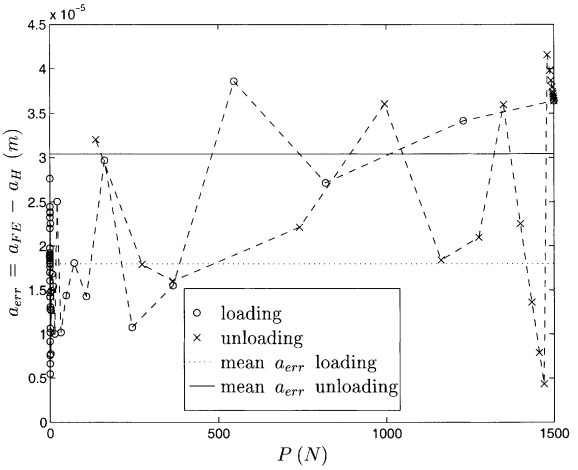

Fig. 9. Error a_{err} in FE contact-area radius a_{FE} for elastic verification.

Table 1
Error $a_{\mathrm{err}} := a_{\mathrm{FE}} - a_{\mathrm{H}}$ for elastic verification

Phase	Max a_{err} (m)	Min a_{err} (m)	Mean a_{err} (m)
Loading	3.86×10^{-5}	5.48×10^{-6}	1.82×10^{-5}
Unloading	4.16×10^{-5}	4.32×10^{-6}	3.04×10^{-5}

loading; 2.67% for unloading. These relative error percentages are consistent with the node-distance method to estimate a_{FE} as described above.

Near $P_3^* = 1500$ N in Fig. 8, the FE curve exhibits a short plateau within which a_{FE} appears to be constant. This plateau occurs due to the small magnitudes of the nodal displacements in comparison with the IRS22A element dimensions. That is, for data points within the plateau, the contact-area radius appears

to be relatively constant because *no new nodes* are being added to the contact. While the contacting nodes do experience small displacements that represent changes in contact-area radius, these displacements are not large enough to show visible changes in a_{FE}.

In summary, in the elastic FEA verification, the normal stress distribution and the NFD relation are not as sensitive to mesh refinement as are the tangential stress distribution and the TFD relation. We attribute this difference to the presence of friction on the contact surface in the tangential loading case. See Section 3.3 for the results of the elastic FEA verification in the tangential direction. The elastic verification analysis required 3.0 min of CPU time on a DEC Alpha 250 workstation with 64 MB of RAM and running DEC Unix 3.2.

2.4. Elasto-plastic analyses

For an estimation of the behavior of elasto-plastic contacting spheres in the normal direction, we consider the von Mises yield criterion as part of the FEA. We apply the loading histories $N1$ through $N3$ and refer to the corresponding elasto-plastic cases as *NEP*1 through *NEP*3, respectively.

Fig. 10 shows the plot of the normal force P against the computed normal displacement α_{FE}. During the P-increasing phase of each loading history, the P versus α_{FE} curve is softer (of lower slope) than is predicted by the Hertzian expression (2.7). For each loading history in Fig. 10, a maximum normal displacement α^* occurs at the maximum normal force P^*. For all loading cases, the plastic flow within the spheres causes this maximum displacement to be greater than is predicted by Hertz theory. Table 2 lists the maximum displacements for the elasto-plastic analyses.

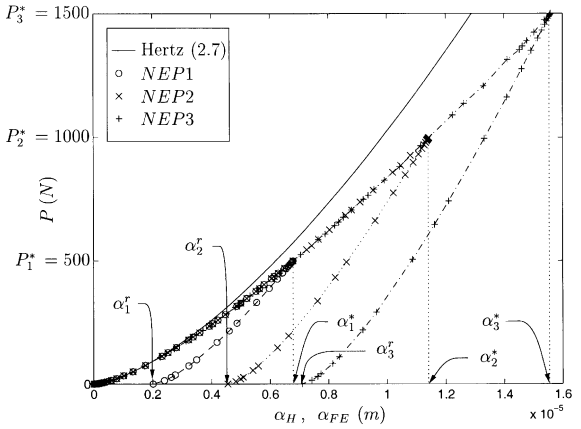

Fig. 10. Normal force P versus normal displacement α_{FE} for axisymmetric elasto-plastic analysis. Hertzian curve given by Eq. (2.7) for both loading and unloading.

Table 2
Maximum and residual displacements, areas and coefficients of restitution for NFD curves of Fig. 10 (elasto-plastic analysis)

Case	α^* (m)	α^r (m)	Area (Nm)	e
*NEP*1	6.69×10^{-6}	2.01×10^{-6}	4.17×10^{-4}	0.841
*NEP*2	1.14×10^{-5}	4.55×10^{-6}	1.94×10^{-3}	0.776
*NEP*3	1.56×10^{-5}	7.10×10^{-6}	4.58×10^{-3}	0.738

At the instant that P^* occurs, unloading begins and the normal displacement decreases. Because permanent plastic strain occurs within the spheres, the unloading P versus α_{FE} relationship is not the same as that for loading. Some energy dissipation occurs as a result of the plastic deformation (damage) in the material. Consequently, at the end of unloading, when the normal force P returns to zero, a non-zero residual displacement α^{r} remains. The magnitude of α^{r} increases with the magnitude of P^* as higher maximum force levels cause more permanent damage. See Table 2 for a list of the residual displacements for the elasto-plastic analyses.

An additional measure of the damage to the spheres is the area that is contained within the NFD (P versus α) curves. The contained area is equal to the energy that is dissipated during the complete load–unload cycle. In terms of the areas, we formulate the classical coefficient of restitution e as

$$e = \sqrt{\frac{\text{area under unloading curve}}{\text{area under loading curve}}}. \tag{2.16}$$

Equivalently, the coefficient e is simply the fraction of energy that is returned at the end of a complete load–unload cycle. Table 2 shows the areas and coefficients of restitution corresponding to the NFD curves of Fig. 10.

Note that, as shown in Table 2, the coefficients of restitution for the FE cases under consideration decrease as the maximum normal force increases. From a dynamic standpoint (i.e., as opposed to quasi-static) the maximum normal force exerted between colliding spheres increases as relative incoming velocity of the spheres increases. The decrease of coefficient e with increasing incoming velocity has been verified experimentally by Goldsmith (1960).

Fig. 11 shows, for the elasto-plastic analysis, the normal pressure p_{FE} that is exerted on the IRS22A elements at the three values of maximum normal force level P^*. Note that the plastic flow in the spheres causes the normal pressure profiles to be flattened to values that are below the Hertz pressure. In each case, the normal pressure p_{FE} appears to be distributed over a contact-area with a radius that is larger than the Hertz radius.

The anomalous data point at $r = 0$ in Fig. 11 appears for all three normal force levels at a normal pressure of approximately 1×10^8 N/m^2. This anomaly is attributed to the finite element method employed

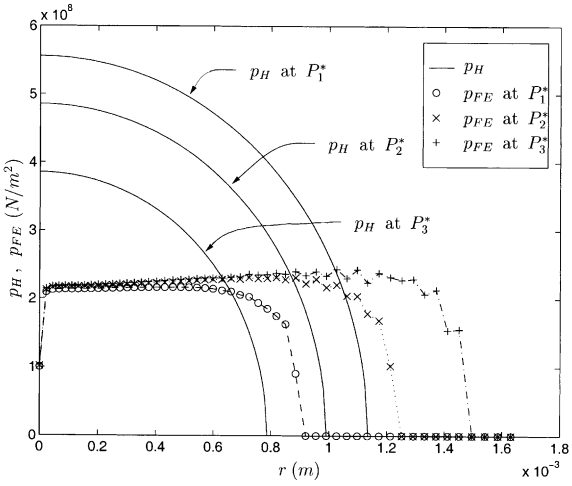

Fig. 11. Normal pressure p_{FE} exerted on IRS22A elements for axisymmetric elasto-plastic analysis. *Flattening* of pressure profile and increase of contact-area.

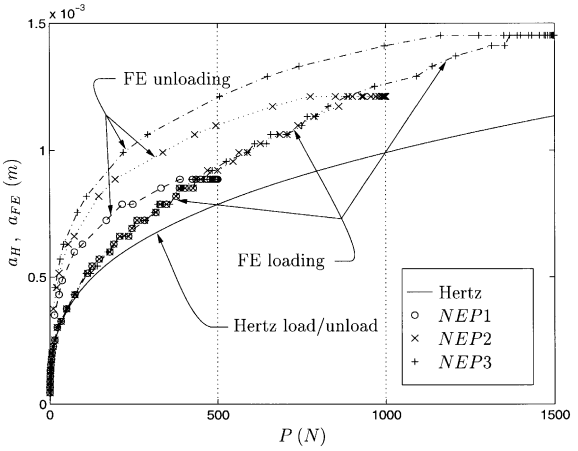

Fig. 12. Contact area radius a_{FE} versus normal force P for axisymmetric elasto-plastic analysis.

to analyze this problem. While this anomalous pressure value is equal to the material yield stress σ_{Y}, we consider this fact to be coincidental. In a similar analysis with $\sigma_{\mathrm{Y}} = 2 \times 10^8$ N/m^2, we did not observe the anomalous point to be at a normal pressure of 2×10^8 N/m^2. In addition, recall that a similar data point appeared in the *elastic* verification of Fig. 7, in which we did not consider elasto-plasticity.

Fig. 12 shows, for the elasto-plastic analysis, the contact-area radius a_{FE} plotted against the applied normal force P. We once again use the node-distance method to determine the contact-area radius a_{FE}. During the loading phase of each elasto-plastic case, a_{FE} increases to values that are consistently greater than those given by the Hertz expression (2.5). As the normal force increases, so does the difference $a_{\mathrm{FE}} - a_{\mathrm{H}}$. At all values of the normal force P, the difference $a_{\mathrm{FE}} - a_{\mathrm{H}}$ for the elasto-plastic cases is larger than the same difference obtained in the elastic verification. The reason for the larger contact-area radii in the elasto-plastic case is the plastic deformation (and *not* the overestimation of the contact-area radius a_{FE} due to the use of the node-distance method).

Near the termination of each loading phase as shown Fig. 12, the a_{FE} versus P curves reach a plateau that is similar to that presented in Fig. 8. We attribute such behavior once again to the relatively small nodal displacements at the contact. Even under plastic deformation, the nodal displacements are not large compared to the element dimensions.

During the unloading phase of each elasto-plastic case, Fig. 12 shows that the a_{FE} versus P relationship is not the same as that during the loading phase. In fact, the difference between a_{FE} and a_{H} during unloading does not vary significantly over almost the entire range of the normal force values. This observation is *critical* in the successful construction of our elasto-plastic NFD model.

By identifying and quantifying trends in the previous FEA results, we can begin to develop a new NFD model for the contact of elasto-plastic spheres. While we describe this NFD model in complete detail in Vu-Quoc et al. (2000b) and in Vu-Quoc and Zhang (1999), we include below a brief discussion of the relevant data reduction that is at the foundation of this accurate and efficient elasto-plastic NFD model.

We define the elasto-plastic contact-area radius a^{ep} as the radius of the circular contact-area that exists between elasto-plastic spheres in normal contact. We assume that a^{ep} may be decomposed additively as

$$a^{\mathrm{ep}} = a^{\mathrm{e}} + a^{\mathrm{p}}, \tag{2.17}$$

where a^{e} is the elastic (Hertzian) part of the contact-area radius and a^{p} the plastic correction part. For a normal force P applied to two contacting elasto-plastic spheres, the elastic contact-area radius a^{e} is given by the Hertz expression (2.5). Taking the computed contact-area radius a_{FE} as an estimate for the elasto-plastic

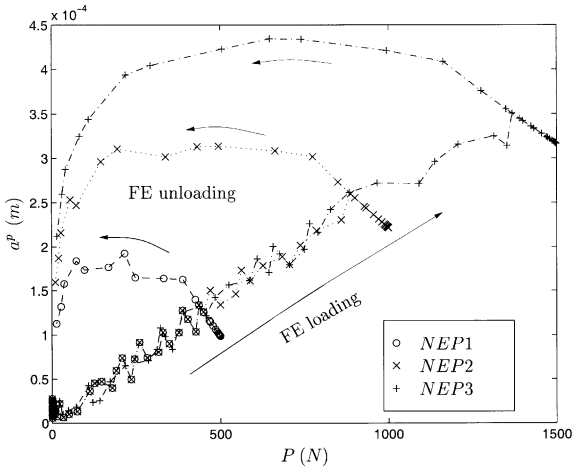

Fig. 13. Plastic correction a^{p} of elasto-plastic contact-area radius $a^{\mathrm{ep}} \approx a_{\mathrm{FE}}$ for the axisymmetric elasto-plastic analysis.

contact-area radius a^{ep} for the spheres and loading histories in the present study, we can compute the plastic correction part a^{p} of the contact-area radius as follows

$$a^{\mathrm{p}} = a_{\mathrm{FE}} - a_{\mathrm{H}}. \tag{2.18}$$

In Fig. 13, we plot the computed plastic correction $a^{\mathrm{p}} = a_{\mathrm{FE}} - a_{\mathrm{H}}$ versus the normal force P for this elasto-plastic analysis. The increase of a^{p} during loading appears to be roughly linear up to the largest maximum normal force P_3^*. When unloading begins at each value of P^*, a^{p} shows an immediate increase that is the result of the plateaus that appear in Fig. 12. Following this brief increase, there is an interval in which a^{p} is roughly constant until near the end of unloading, where a^{p} shows a steep decrease.

Given our definition of a^{p} as the *plastic* correction part of the contact-area radius a^{ep}, we expect a^{p} to be non-zero only for normal forces of magnitude *greater* than P_{Y} during the first virgin loading. This supposition is further supported by the observation that a^{p} in Fig. 13 shows a linear increase only after a brief interval of small normal force values. To describe a^{p} as a function of the normal load P, we make use of the MacCauley bracket defined by

$$\langle x \rangle = \begin{cases} 0 & \text{for } x \leqslant 0 \\ x & \text{for } x > 0 \end{cases}. \tag{2.19}$$

Based on the above observation, we approximate the behavior of the plastic correction part a^{p} by the following expression

$$a^{\mathrm{p}}(P) = k_{\mathrm{a}} \langle P - P_{\mathrm{Y}} \rangle, \tag{2.20}$$

where k_{a} is a constant that depends on the spheres' material and geometric properties. The meaning of Eq. (2.20) is clear: Plastic correction of the contact-area radius occurs only for normal load P beyond the yield normal load P_{Y}.

To determine the constant k_{a}, we perform a least squares fit of the loading data for the elasto-plastic case *NEP*3. We use Matlab's built-in function `nlinfit.m`, which employs the Gauss–Newton (GN) method. For the FE data of the current investigation, the curve fit yields the constant $k_{\mathrm{a}} = 2.33 \times 10^{-7}$ m/N.

In Fig. 14, we show the linear curve fit together with the FE data of the loading phase of *NEP*3. Since we take the independent variable to be $\langle P - P_{\mathrm{Y}} \rangle$, the figure does not show data points for $P < P_{\mathrm{Y}}$. Note that the fitted curve is significantly lower than the FE data that is shown. We attribute this under approximation to

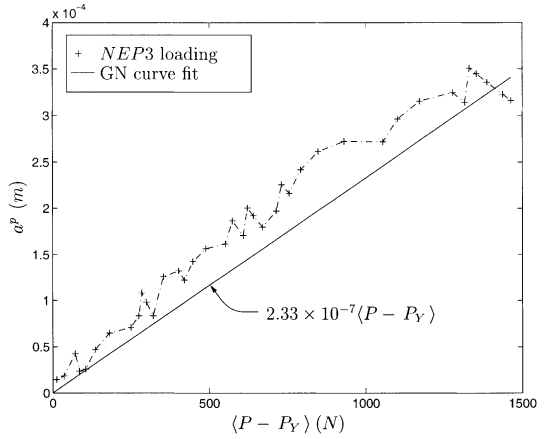

Fig. 14. GN curve fit of a^{p} data for *NEP*3 loading.

the fact that we force the fitted curve to pass through the origin in Fig. 14. That is, the FE data may be better approximated by a linear function

$$a^{\mathrm{p}}(P) = k_{\mathrm{a}}^{(0)}\langle P - P_{\mathrm{Y}}\rangle^0 + k_{\mathrm{a}}^{(1)}\langle P - P_{\mathrm{Y}}\rangle^1, \tag{2.21}$$

where $k_{\mathrm{a}}^{(0)}$ is an additional constant. This form of the fitted curve, however, implies that $a^{\mathrm{p}}(P)$ becomes nonzero at the instant that $P > P_{\mathrm{Y}}$, thus causing a discontinuous transition between elastic and plastic regimes. Recall also that the FE data of Fig. 14 is likely shifted up due to the overestimation of a_{FE} that is part of the node-distance method. Given this erroneous upward shift of the data, we choose to omit the constant $k_{\mathrm{a}}^{(0)}$. We note that the final results using Eq. (2.20) in our NFD model – for both the displacement-driven version (Vu-Quoc and Zhang, 1999) and the force-driven version (Vu-Quoc et al., 2000b) – are accurate.

Fig. 15 shows the plot of normal displacement α_{FE} versus contact-area radius a_{FE} for the elasto-plastic analysis. The plot also includes the parabolic Hertzian relationship (2.6) for comparison. During the

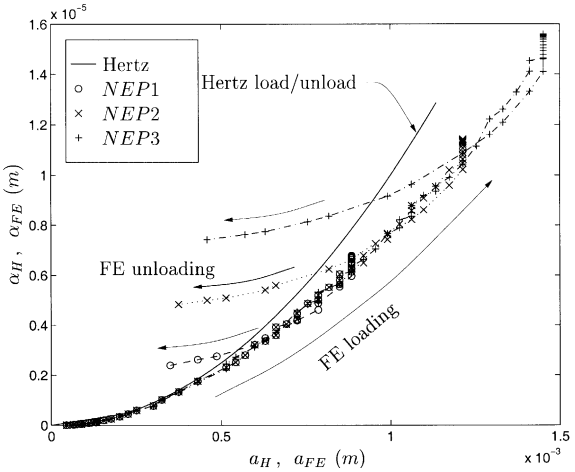

Fig. 15. Normal displacement α_{FE} versus contact-area radius a_{FE} for axisymmetric elasto-plastic analysis. Hertz expression given by Eq. (2.6).

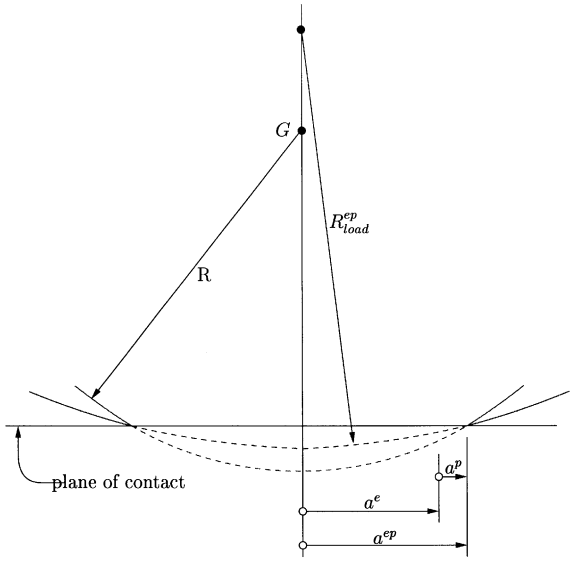

Fig. 16. Plastic deformation causes increase in radius of curvature local to the contact-area.

loading portion of each elasto-plastic case, for $P > P_Y$, for a given normal displacement α, the elasto-plastic contact-area radius a_{FE} is larger than the elastic Hertzian contact-area radius a_H, and this difference grows gradually larger as the normal load P increases well beyond P_Y. During unloading, the permanent deformation of the material causes the α_{FE} versus a_{FE} relationship to be different from that obtained during loading. Each unloading curve terminates at a point that defines the residual displacement α^r and residual contact-area radius a_r.

As plastic flow occurs during the loading phase, there is a "flattening" of the sphere at the contact point, resulting in an increase in the radius of curvature at the contact point. We use the symbol R^{ep}_{load} to designate this *elasto-plastic* radius of curvature for the loading phase. Since increasing normal force causes increasing plastic flow, we expect R^{ep}_{load} to increase with the quantity $\langle P - P_Y \rangle$. Fig. 16 presents a graphical explanation of the flattening of the sphere due to plastic flow in the loading phase.

To model the relationship among the normal displacement α_{FE}, the contact-area radius a_{FE}, and the radius of curvature R^{ep}_{load}, for the elasto-plastic loading cases, we consider equivalent *elastic* spheres with radii of curvature R^{ep}_{load}, and such that Hertzian relationships hold among the quantities α_{FE}, a_{FE}, and R^{ep}_{load}.

The parabolic Hertz expression (2.6) relates the normal displacement α to the contact-area radius a in the form

$$\alpha = \frac{a^2}{R}.$$

Assuming that a parabolic relationship similar to Eq. (2.6) applies for the equivalent elastic spheres, we seek an expression of the form

$$\alpha_{FE} = \frac{(a_{FE})^2}{R^{ep}_{load}} \tag{2.22}$$

that approximates the *loading* part of the FE curve of Fig. 15. To accommodate the increase of R^{ep}_{load} with normal force, we propose the relationship

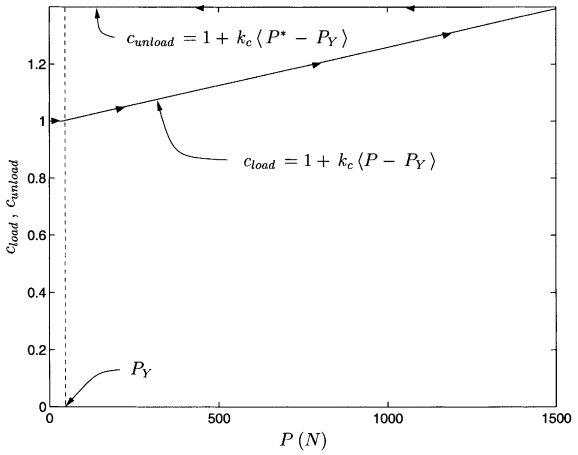

Fig. 17. Variation of c_{load} and c_{unload}.

$$R^{\text{ep}}_{\text{load}} = c_{\text{load}} R, \tag{2.23}$$

where $c_{\text{load}} \geqslant 1$ is a dimensionless coefficient that indicates the amount of increase in the radius of curvature due to plastic flow. Based on our observation of the numerical results, we approximate the relationship between the coefficient c_{load} and the normal force P as follows

$$c_{\text{load}} = 1 + k_{\text{c}} \langle P - P_{\text{Y}} \rangle, \tag{2.24}$$

where k_{c} may depend on the geometric and material properties of the spheres. Note that Eq. (2.24) gives $c_{\text{load}} = 1$ for $P < P_{\text{Y}}$, implying that $R^{\text{ep}}_{\text{load}} = R$ when plastic flow does not occur. Fig. 17 shows the variation of c_{load} with the normal force P.

Combining Eqs. (2.22) through (2.24), we obtain

$$\alpha_{\text{FE}} = \frac{(a_{\text{FE}})^2}{(1 + k_{\text{c}} \langle P - P_{\text{Y}} \rangle) R}, \tag{2.25}$$

where k_{c} remains unknown. Using once again function `nlinfit.m`, we fit Eq. (2.25) to the loading data of *NEP*3 for $P > P_{\text{Y}}$. The curve fit results in $k_{\text{c}} = 2.69 \times 10^{-4}$ N^{-1}; a substitution of this value of k_{c} into Eq. (2.25) yields the curve shown in Fig. 18.

Note that the constant k_{c} needs only be determined for the *loading* of the elasto-plastic spheres. At the start of unloading, we assume that plastic flow effectively ceases and that the unloading radius of curvature $R^{\text{ep}}_{\text{unload}}$ takes the value of $R^{\text{ep}}_{\text{load}}$ from the termination of the loading. That is, during *unloading* from a *maximum* normal force P^*, we have

$$R^{\text{ep}}_{\text{unload}} = c^*_{\text{load}} R, \tag{2.26}$$

where

$$c^*_{\text{load}} = 1 + k_{\text{c}} \langle P^* - P_{\text{Y}} \rangle. \tag{2.27}$$

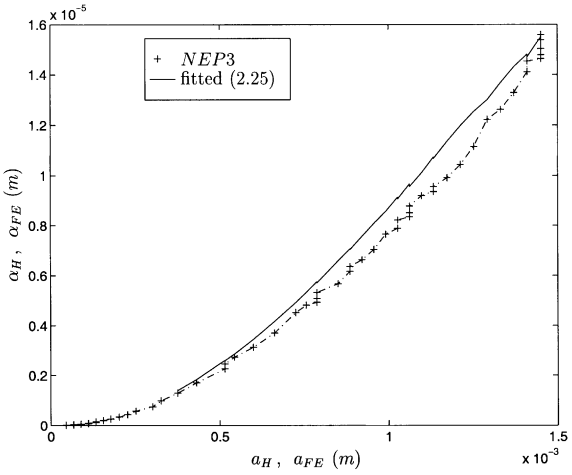

Fig. 18. Normal displacement α_{FE} versus contact-area radius a_{FE} for loading. Fitted expression (2.25) and loading data for *NEP*3.

The constant c^*_{load} is the value of c_{load} at the end of the loading phase. For parallelism with the loading notation, we rewrite Eq. (2.26) as

$$R^{\mathrm{ep}}_{\mathrm{unload}} = c_{\mathrm{unload}} R, \tag{2.28}$$

where $c_{\mathrm{unload}} = c^*_{\mathrm{load}}$. Fig. 17 shows the variation of c_{unload} with P^*.

To fit a curve through the unloading part of the FE data in Fig. 15, it is not sufficient to simply substitute $R^{\mathrm{ep}}_{\mathrm{unload}}$ into an expression of the form Eq. (2.22). We must account for the residual displacement α^{r} that remains at the end of each unloading phase. To this end, we propose that the difference $(\alpha_{\mathrm{FE}} - \alpha^{\mathrm{r}})$ is related to the elastic part a^{e} of the total contact-area radius in the manner

$$\alpha_{\mathrm{FE}} - \alpha^{\mathrm{r}} = \frac{(a^{\mathrm{e}})^2}{R^{\mathrm{ep}}_{\mathrm{unload}}}, \tag{2.29}$$

where $R^{\mathrm{ep}}_{\mathrm{unload}}$ is calculated from Eq. (2.28) and a^{e} is given by the Hertz expression (2.5). Note that in Eq. (2.29), we relate $(\alpha_{\mathrm{FE}} - \alpha^{\mathrm{r}})$ to a^{e} since we consider the plastic part a^{p} of a_{FE} to be fixed during unloading and *not recoverable*.

To compute the residual displacement α^{r} in Eq. (2.29), we consider the turning point where the displacement α^* is known from the loading portion of the fitted curve. To determine the elastic contact-area radius a^{e}_* at the turning point, we substitute P^* into Eq. (2.5). Substituting a^{e}_* and α^* into Eq. (2.29), we solve for the residual displacement to obtain

$$\alpha^{\mathrm{r}} = \alpha^* - \frac{(a^{\mathrm{e}}_*)^2}{R^{\mathrm{ep}}_{\mathrm{unload}}}. \tag{2.30}$$

By substituting Eq. (2.30) into Eq. (2.29), we determine an expression for the *unloading* curves shown in solid lines in Fig. 19.

The execution times for the elasto-plastic analysis increase with the maximum normal force. On a DEC Alpha 250 workstation with 64 MB of RAM and running DEC Unix 3.2, elasto-plastic cases *NEP*1, *NEP*2, *NEP*3 require 3.4, 5.2, and 5.8 min of CPU time, respectively.

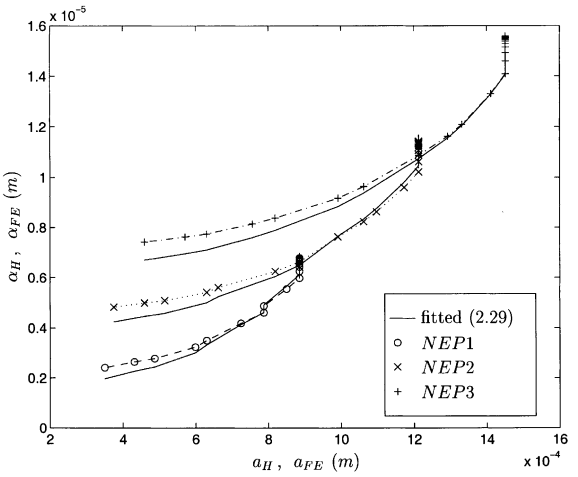

Fig. 19. Normal displacement α_{FE} versus contact-area radius a_{FE} for unloading. Fitted expression (2.29) and loading data for *NEP*1 through *NEP*3.

3. Tangential FD relation

3.1. Tangential contact mechanics theories

Fig. 20 shows two identical spheres in frictional contact and subjected to normal force P and tangential force Q. Existing theories for such a contact address two problem domains: P constant, Q varying; P and Q varying. In this section, we summarize the principles and results of these two subclasses of contact.

3.1.1. P constant, Q varying

The problem of P constant and Q varying was solved independently by both Cattaneo (1938a,b,c) and Mindlin (1949). Each addressed the problem under the following assumptions:

- Hertzian normal pressure on the contact surface.
- Effects of normal and tangential force can be treated independently.
- Complete *sticking* on the contact surface will cause the tangential stress distribution to go infinity at the edge of contact.

The final assumption above introduces the concept of *slip*, which alleviates the otherwise infinite tangential stress at the edge of the contact-area. Fig. 21(a) shows the *slip area*, an annulus $c \leqslant r \leqslant a$ in which the tangential stress q is the friction limit $q_{\mathrm{m}} = \mu p$. The inner radius c of the slip region is known as the *slip radius*, and approaches zero as the applied tangential force approaches $Q_{\mathrm{m}} = \mu P$.

Cattaneo (1938a,b,c) and Mindlin (1949) each applied a superposition method to determine the tangential stress q on the contact-area. (Johnson (1985) refers to this method as *Cattaneo's technique*.) The result of the superposition is the stress distribution q shown in Fig. 21(b). The stress profile is given by

$$q = \begin{cases} \dfrac{3\mu P}{2\pi a^3}\left(a^2 - r^2\right)^{1/2}, & c \leqslant r \leqslant a, \\ \dfrac{3\mu P}{2\pi a^3}\left[\left(a^2 - r^2\right)^{1/2} - \left(c^2 - r^2\right)^{1/2}\right], & r \leqslant c. \end{cases} \tag{3.1}$$

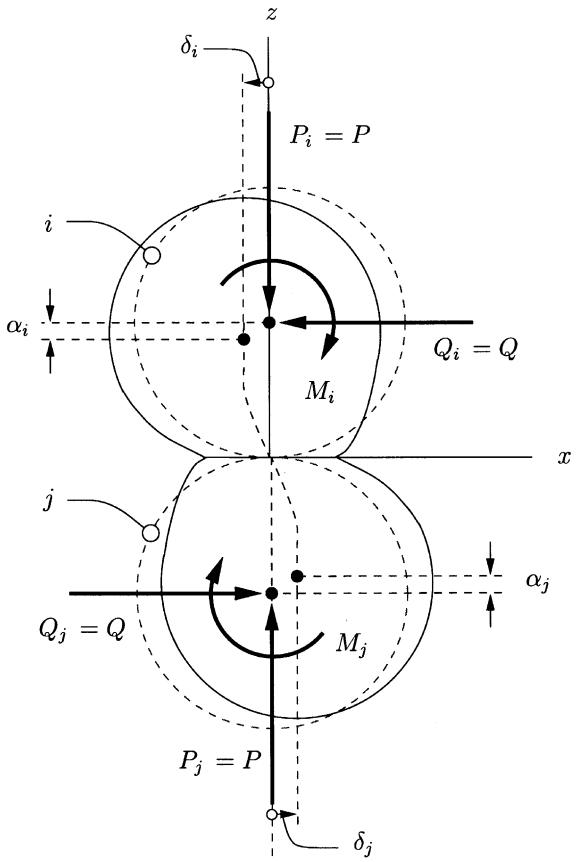

Fig. 20. Two frictional spheres subjected to normal and tangential forces. (Moments M_i and M_j are required to maintain equilibrium.)

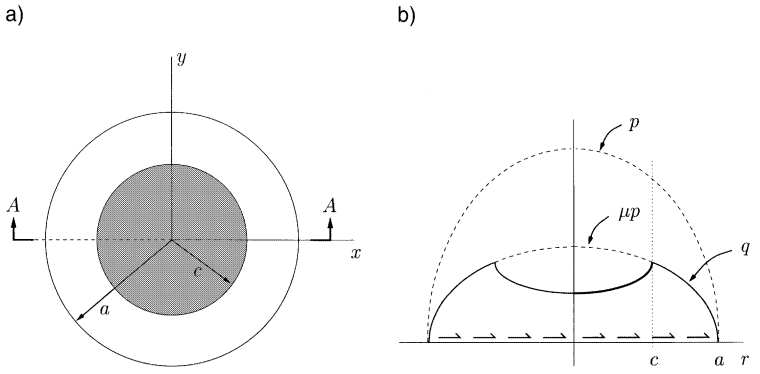

Fig. 21. Slip region and tangential stress distribution. (a) Annulus of slip. Section *A–A* is aligned with a contact-area diameter. (b) Tangential stress on the contact-area, at section *A–A*.

By integrating Eq. (3.1) over the contact-area and setting the result equal to the applied tangential force, Cattaneo (1938a,b,c) and Mindlin (1949) arrived at the following expression for the slip radius:

$$c = a\left(1 - \frac{Q}{\mu P}\right)^{1/3}. \tag{3.2}$$

From the above expression, one observes that the slip region is nonexistent (i.e., $c = a$) only when $Q = 0$, or when the tangential force is not applied.

By considerations of displacements due to slip and stick, Mindlin (1949) determined the net displacement of the spheres relative to the contact-area as follows

$$\delta = \frac{3(2-\nu)\mu P}{16Ga}\left[1 - \left(1 - \frac{Q}{\mu P}\right)^{2/3}\right], \tag{3.3}$$

where G is the shear modulus. To determine the tangential compliance c_{T} for the contact, Mindlin (1949) differentiated Eq. (3.3) with respect to Q to obtain

$$c_{\mathrm{T}} := \frac{\partial\delta}{\partial Q} = \frac{2-\nu}{8Ga}\left(1 - \frac{Q}{\mu P}\right)^{-(1/3)} \qquad (P \text{ constant}, Q \nearrow), \tag{3.4}$$

which is the inverse of the tangential stiffness K_{T}, given by

$$K_{\mathrm{T}} := \frac{1}{c_{\mathrm{T}}} = \frac{8Ga}{2-\nu}\left(1 - \frac{Q}{\mu P}\right)^{1/3}. \tag{3.5}$$

While Eq. (3.3) does provide tangential displacement explicitly in terms of tangential force, such an expression is possible only because the normal force is constant. In cases of varying normal force, Eqs. (3.4) and (3.5) provide the foundation for more general *incremental* solutions for tangential displacement.

Using an argument similar to that for the case where Q increases, Mindlin and Deresiewicz (1953) determined expressions for the case of Q-decreasing from some maximum (or *turning point*) tangential force Q^*. The tangential displacement for this case is given by

$$\delta = \frac{3(2-\nu)\mu P}{16Ga}\left[2\left(1 - \frac{Q^* - Q}{2\mu P}\right)^{2/3} - \left(1 - \frac{Q}{\mu P}\right)^{2/3} - 1\right], \tag{3.6}$$

where a is the contact-area radius, which is a constant since P is unchanging. Differentiating once again with respect to Q, one can obtain compliance and stiffness expressions for Q-decreasing. The expression for the compliance is shown below, while that for the stiffness (the inverse) is left to the reader.

$$c_{\mathrm{T}} = \frac{2-\nu}{8Ga}\left(1 - \frac{Q^* - Q}{2\mu P}\right)^{-(1/3)} \qquad (P \text{ constant}, Q \searrow). \tag{3.7}$$

Fig. 22 summarizes the relationship between Q and δ for the case of constant normal load. Note that, as indicated by Eq. (3.6), a residual displacement δ_{r} exists at $Q = 0$ in the Q-decreasing phase of the loading history. This residual displacement is a result of the energy loss that occurs due to the presence of friction on the contact-area. In addition, the energy loss causes the Q–δ plot to take the form of a hysteresis loop, with the same amount of energy lost during each complete loading cycle.

3.1.2. P varying, Q varying

The problem of varying normal and tangential forces was solved in Mindlin and Deresiewicz (1953). These authors applied an incremental method to determine tangential-compliance expressions for different cases of varying P and Q. To develop our TFD model, we consider the following two frequent cases:

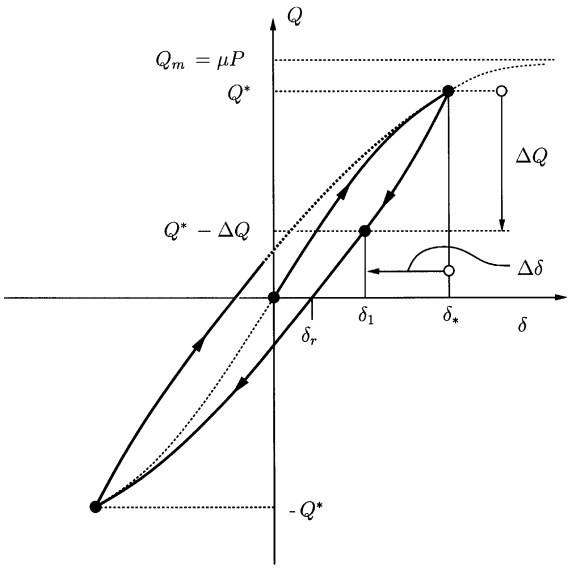

Fig. 22. TFD plot for case of P-constant, Q-varying. Hysteresis loop and residual displacement.

- P and Q both increasing, which would occur during many loading phases.
- P and Q both decreasing, which would occur during many unloading phases.

The analysis of Mindlin and Deresiewicz (1953) is complex, so we refer the reader to the original paper for the details. Additional helpful references are Johnson (1985), Jaeger (1992, 1999).

For the case of P and Q both increasing, Mindlin and Deresiewicz (1953) determined two compliance expressions shown below

$$c_{\mathrm{T}} = \frac{2-\nu}{8Ga}\left[\mu\frac{\mathrm{d}P}{\mathrm{d}Q} + \left(1-\mu\frac{\mathrm{d}P}{\mathrm{d}Q}\right)\left(1-\frac{Q}{\mu P}\right)^{-(1/3)}\right], \quad 0 \leqslant \frac{\mathrm{d}P}{\mathrm{d}Q} \leqslant \frac{1}{\mu}, \tag{3.8}$$

$$c_{\mathrm{T}} = \frac{2-\nu}{8Ga}, \quad \frac{\mathrm{d}P}{\mathrm{d}Q} \geqslant \frac{1}{\mu}. \tag{3.9}$$

Note that, in the above expressions, $\mathrm{d}P/\mathrm{d}t > 0$, which implies that a is not a constant as it is in Cattaneo's analysis.

For the case of P and Q both decreasing, Mindlin and Deresiewicz (1953) determined the following tangential compliance expression:

$$c_{\mathrm{T}} = \frac{2-\nu}{8Ga}\left[-\mu\frac{\mathrm{d}P}{\mathrm{d}Q} + \left(1+\mu\frac{\mathrm{d}P}{\mathrm{d}Q}\right)\left(1-\frac{Q^*-Q}{2\mu P}\right)^{-(1/3)}\right], \quad \frac{\mathrm{d}P}{\mathrm{d}Q} \geqslant 0 \tag{3.10}$$

(Mindlin and Deresiewicz (1953) did determine another compliance expression for the case of P and Q both decreasing. This expression applies for $Q = Q^*$, and is not discussed here.)

3.2. Finite-element model for tangential contact

Recall that in Section 2.2 we applied a frictionless rigid surface to represent the plane of symmetry that exists at the contact plane between two identical spheres subjected to a normal load. While we studied only frictionless spheres in that analysis, this symmetry condition exists even for frictional spheres as long as they are identical in radii and material properties and subjected to only a normal load.

In the case of identical frictional spheres subjected to normal and tangential loads, it is not possible to apply this symmetry condition in general. First, to avoid rigid body motion of the spheres, the rigid surface would have to be frictional at least while the tangential force is applied. Second, a frictional rigid surface would induce tangential stress at the spheres' surfaces *even under normal loading without a tangential force*. One can derive artificial loading histories and material behaviors that avoid these pitfalls, but these special cases are few in number and are not representative of real contacts. (One example is normal loading without friction followed by tangential loading with friction and constant normal load.)

Considering the above restrictions, we study the case of oblique loading by actually modeling the two contacting deformable solids; the rigid contact surface is omitted. By invoking the Saint Venant principle, we limit the domain of FE discretization to the gray domains shown in Fig. 23. We model only the region closest to the contact-area, since Hertz theory shows that stresses decrease rapidly away from the contact-area and toward the centers of the spheres. The geometric and elastic sphere properties are identical to those used in the normal loading analysis ($R = 0.1$ m, $E = 7.0 \times 10^{10}$ N/m^2, $\nu = 0.3$). In the elasto-plastic analysis, we consider, however, two yield stress values: $\sigma_Y = 1.0 \times 10^8$ N/m^2 (also used in the normal analysis); and $\sigma_Y = 2.0 \times 10^8$ N/m^2.

We clamp the upper surface s_i of the upper solid (Fig. 23), and apply all loads to the lower surface s_j of the lower solid. We constrain all points on s_j to undergo identical displacements, producing the effect of

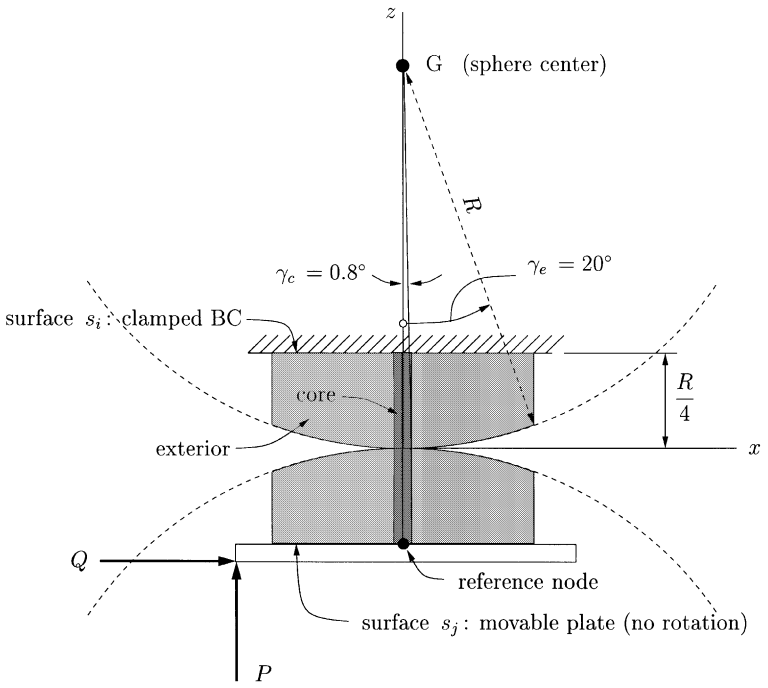

Fig. 23. Domain of FE discretization analysis for oblique force loading.

loads applied to a rigid surface without rotation. Note that this rigid surface is only a boundary condition, serving to transmit loads to the solids. It is not involved in the contact constraints as in the case of normal loading. Although we do not require a rigid-surface reference node as in the normal loading case, we do designate one node as an informal reference and measure all displacements at this location. This node is indicated in Fig. 23.

We divide each solid (gray zone in Fig. 23) in the current analysis into two major subdomains. The *core* of each solid, with highly refined FE mesh, is defined by the *core construction angle* $\gamma_c = 0.8°$. The exterior of each solid, with less refined FE mesh, is defined by the *exterior construction angle* $\gamma_e = 20°$. We carefully choose loading histories such that the contact occurs entirely within the surfaces of the core regions with highly refined FE mesh; the exterior regions are not involved in the contact.

Fig. 24 shows an isometric view of the FE discretization of the gray zones in Fig. 23. The model contains a total of 3420 C3D8 elements (1710 for each solid), where the C3D8 designation specifies a 3D element having eight nodes and eight integration points (i.e., an eight-noded brick or hexahedral element). The current mesh represents a system with 15,114 equations and, after applying the Cuthill–McKee node renumbering, a bandwidth of 168.

To convey the degree of discretization in the current mesh, we once again compare the average edge length of an element near the contact with that of an element far from the contact. Fig. 25(a) shows element Ω_1, which is far from the contact-area, and has an average edge length of 113×10^{-4} m $\approx R/9$. In comparison, Fig. 25(b) shows element Ω_2, which is near the contact-area, and has an average edge length of 2.25×10^{-4} m $\approx R/444$.

We enforce the contact constraint by specifying in the ABAQUS input file that the two deformable solids (gray zones in Fig. 23) make up a `CONTACT PAIR`. For each node on the first surface of the contact pair, ABAQUS attempts to find the closest point on the second surface of the contact pair where the normal to that surface passes through the node. ABAQUS then discretizes the interaction between this point on the second surface and the node on the first (see Hibbitt et al., 1995; Chapter 5).

Figs. 26 and 27 show the loading histories $O1$ and $O2$ for the present analysis with oblique forces. The two loading histories actually demonstrate four cases of oblique loading:

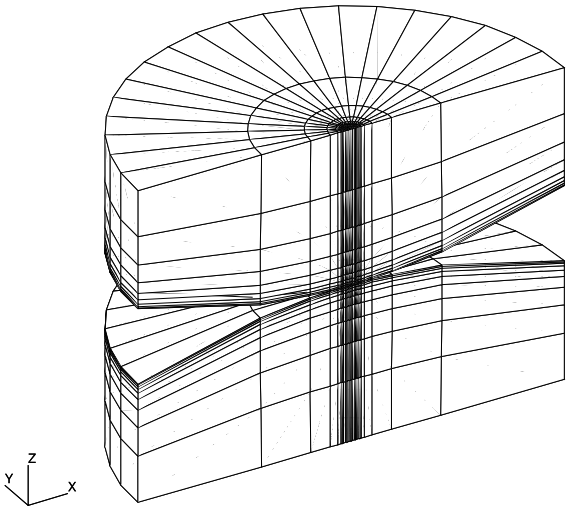

Fig. 24. Discretization used in our study of oblique contact.

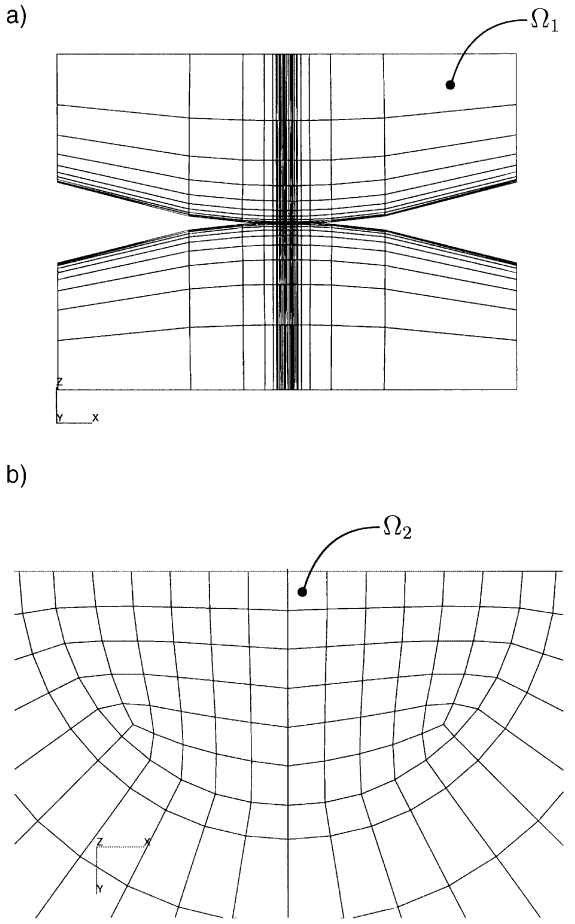

Fig. 25. Degree of discretization for current FE mesh. (a) View of discretization from $-y$. Element Ω_1 average edge length approximately $R/9$. (b) View of discretization from $-z$ (lower solid not shown). Element Ω_2 average edge length approximately $R/444$.

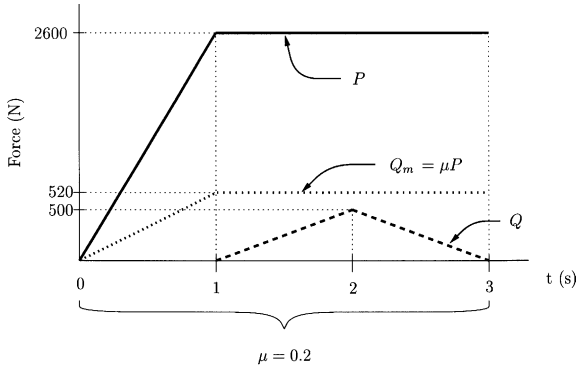

Fig. 26. Loading history $O1$: P-constant, Q-varying.

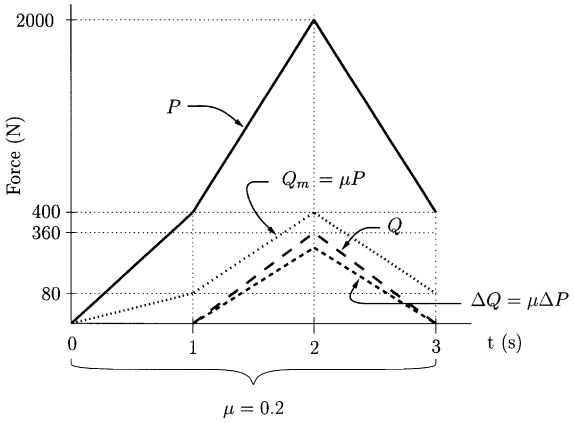

Fig. 27. Loading history $O2$: both P and Q varying.

- P-constant, Q-increasing ($O1$, $t = [1, 2]$);
- P-constant, Q-decreasing ($O1$, $t = [2, 3]$);
- P-increasing, Q-increasing ($O2$, $t = [1, 2]$);
- P-decreasing, Q-decreasing ($O2$, $t = [2, 3]$).

Note that loading history $O1$ includes friction during the application of the normal load. The presence of friction during this phase of the loading is permitted because we model two identical spheres, rather than a single sphere and a rigid surface. Note also that loading history $O2$ is a *simple loading history*, defined in Definition 3.1.

Definition 3.1. (*simple loading history*). A simple loading history is a loading history in which the rate of change of tangential force Q always exceeds the rate of change of the quantity μP. Since μ is typically a constant, a simple loading history is defined by

$$\left|\frac{\mathrm{d}Q}{\mathrm{d}t}\right| \geqslant \mu \left|\frac{\mathrm{d}P}{\mathrm{d}t}\right|, \tag{3.11}$$

or, in terms of force increments, $|\Delta Q| \geqslant \mu |\Delta P|$.

In terms of the methodology of Mindlin and Deresiewicz (1953), a simple loading history is one in which, after each application of the increments of P and Q, the tangential stress distribution is similar to the one obtained in Cattaneo's elastic-frictional contact analysis of tangential loading under constant normal force. Thus, for cases with Q-increasing, for example, the tangential stress distribution must resemble that given by Eq. (3.1). (We have not presented Cattaneo's tangential stress distribution for P-constant and Q-decreasing, see Johnson, 1985.)

3.3. FEA calibration

To calibrate the FE model for oblique loading, we apply loading histories $O1$ and $O2$ to contacting spheres with purely elastic properties. That is, we run the ABAQUS analysis without consideration of the von Mises yield condition. (In the normal FEA calibration, one loading history was sufficient to show the

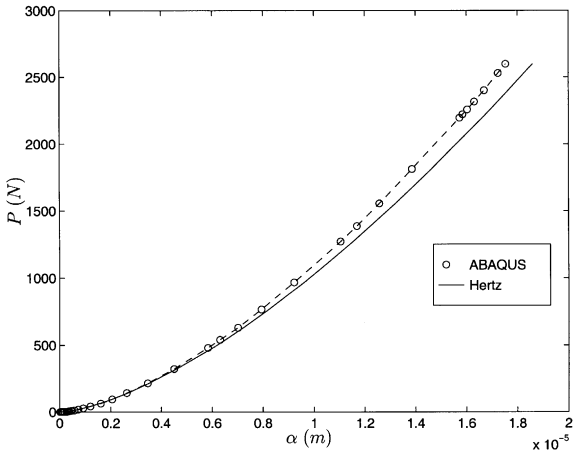

Fig. 28. Normal force P versus normal displacement α for FEA calibration under loading history $O1$.

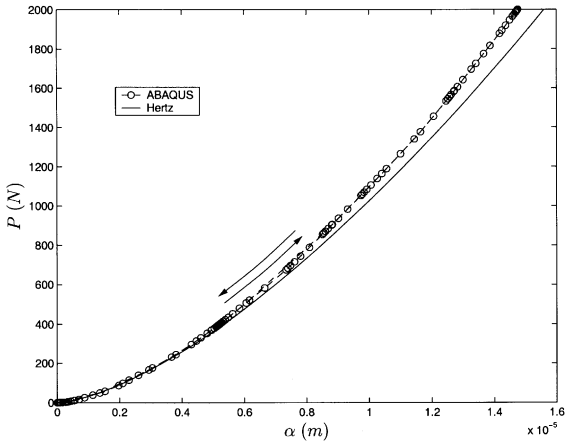

Fig. 29. Normal force P versus normal displacement α for FEA calibration under loading history $O2$.

validity of the FEA mesh. In the oblique FEA, we validate with both loading histories since there are two varying forces.)

Figs. 28 and 29 show the performance of the current FE mesh as it relates to the normal loading history. Both loading histories exhibit close comparison to the Hertz theory, but both also show NFD curves that are stiffer than the elastic contact mechanics prediction. That is, for loading history $O1$, the normal displacement at the maximum normal force is 6% less than the prediction; for loading history $O2$, the normal displacement at the maximum normal force is 5.4% less than the prediction.

Figs. 28 and 29 clearly show that the 3-D FEA model results in NFD predictions that are stiffer than both Hertz theory and axisymmetric FEA. (Recall that, as shown in Fig. 6, the axisymmetric analysis resulted in a maximum NFD deviation of just 0.37%.) We propose the following reasons for the increased stiffness in the 3-D analysis:

- The relatively large aspect ratio of some elements far from the contact-area (see Fig. 24).
- The consideration of subdomains that are too small relative to the size of the contact-area. That is, perhaps either the core construction angle γ_c or the exterior construction angle γ_e need to be increased (see Fig. 23).
- Comparison to NFD results for Hertz's analysis of elastic half-spaces. The half-space analysis cannot be considered exact for either finite objects or large contact-areas.

Figs. 30 and 31 show TFD curves for the current FEA calibration. In both sets of results, the plots are again stiffer than the contact mechanics prediction. For loading history $O1$, the maximum tangential displacement is 2% less than the prediction; for loading history $O2$, the FEA displacement is 1.6% less than the prediction.

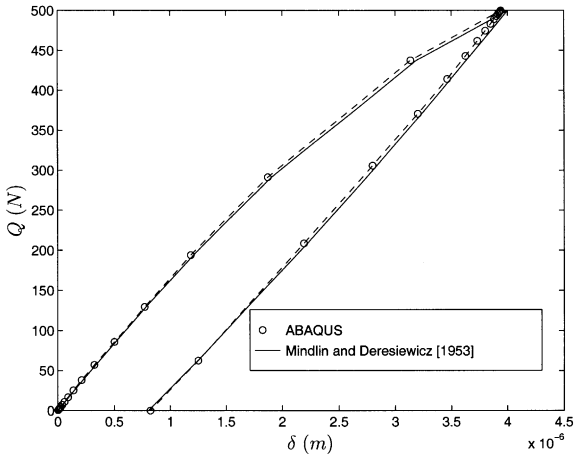

Fig. 30. Tangential force Q versus tangential displacement δ for FEA calibration under loading history $O1$.

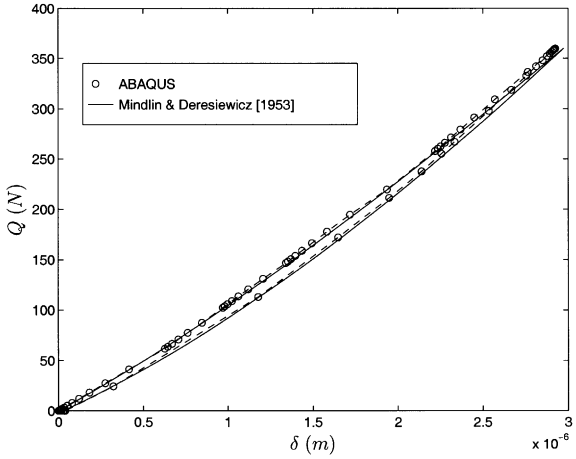

Fig. 31. Tangential force Q versus tangential displacement δ for FEA calibration under loading history $O2$.

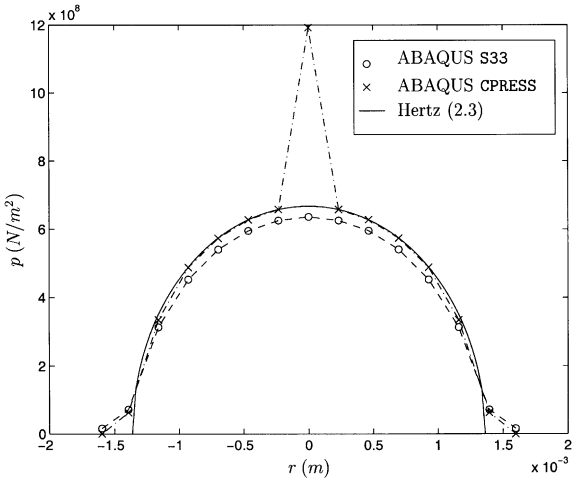

Fig. 32. Normal pressure and principal stress for loading history $O1$ at maximum normal force.

Note that the theoretical solutions in Figs. 28–31 arise from similar foundations of contact mechanics, but are plotted in inherently different ways. The Hertz NFD plots are a result of the application of Eq. (2.7), i.e., the actual NFD equation. The Cattaneo–Mindlin plots, however, result from the repeated application of Eq. (3.5), i.e., the slope of the Cattaneo–Mindlin solution (3.3).

Fig. 32 shows two measurements of stress at the maximum normal force in loading history $O1$. The ABAQUS variable `CPRESS` is the normal contact pressure that is measured during the discretization of the `CONTACT PAIR` contact. The ABAQUS variable `S33` is the principal stress in the direction normal to the contact-area, measured at the nodes of the `C3D8` elements. The results for `CPRESS` closely match the Hertz prediction, with the exception of the stray data point at $r = 0$. Since the plot of `S33` is well-behaved, we attribute this anomalous point to a singularity in the FEA model. (Recall that we observed a similar anomalous point at $r = 0$ in the validation of the axisymmetric FEA model.)

In Fig. 32, the value of `CPRESS` decreases to zero at a radial value that is significantly larger than the Hertz prediction. We attribute this result to the relatively low resolution provided by the contacting elements in the 3-D model. (Recall the much closer prediction that was provided by the more refined but axisymmetric model of the normal direction analysis.) In addition, although `S33` is near zero near the contact radius, this variable is a principal stress and therefore representative of stress *inside* the solid. Consequently, we expect `S33` for this loaded solid to only asymptotically reach zero.

Fig. 33 shows the contact tangential traction `CHSHEAR` at the maximum force level in loading history $O1$. We also show for comparison the shear stress `S13` measured at the nodes of the `C3D8` elements. The plot of `CHSHEAR` matches the theory of Cattaneo (1938a,b,c) and Mindlin (1949), with the exception of the data point at $r = 0$. In addition, similar to `CPRESS` in Fig. 32, the `CHSHEAR` plot shows the same mis-approximation of the contact-area radius.

Note that the plot of `S13` does not exhibit the symmetry that is shown by the plot of `CHSHEAR`. The asymmetry of `S13` is caused by the stage of pure normal loading in loading history $O1$. That is, even without an applied tangential force, normal loading does induce small shear stresses in the spheres near the contact surface. During the application of the tangential force (after the normal force reaches its maximum), shear stresses increase but from non-zero and asymmetric values.

Note that the present calibration analyses resulted in contact areas that were within the bounds of the highly refined core regions. This restriction is advantageous for two reasons. First, the contact occurs within elements that have small edge lengths, thus ensuring improved accuracy over an otherwise coarse

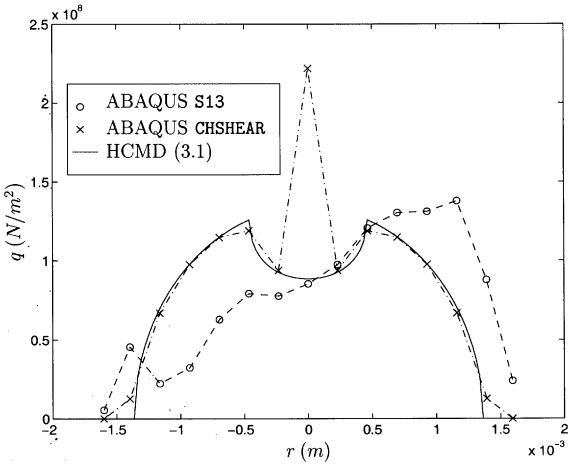

Fig. 33. Tangential traction and shear stress for $O1$ at maximum tangential force.

mesh. Second, the bounds of the core regions correspond to an approximate maximum contact-area of just $R\sin(0.8°) \approx 0.01R$. This small contact-area is in line with Hertz's assumption that the contact-area radius be much smaller than the sphere radius.

In other trial discretizations with larger core regions and larger maximum normal loads, the FD curves did not match well with HCMD theory. In fact, the TFD results in particular showed increased stiffness over the theory and over the present FE mesh.

Loading history $O1$ with elastic material properties required 18.4 min of CPU time on a DEC Alpha 250 workstation with 64 MB of RAM and running DEC Unix 3.2. Under the same conditions, loading history $O2$ required 30.5 min of CPU time.

3.4. Elasto-plastic analysis

To identify the behavior of the FD relationship in the oblique loading of elasto-plastic spheres, we repeat the previous analysis with rate-independent perfect plasticity. As in the normal-loading analysis, we set the material yield stress to $\sigma_Y = 1.0 \times 10^8$ N/m^2, implying that the normal force at yield is $P_Y = 36.4$ N. As an example of a less ductile material, we also run the analysis with $\sigma_Y = 2.0 \times 10^8$ N/m^2, which corresponds to $P_Y = 291.6$ N. Table 3 summarizes the input parameters of the elasto-plastic analyses.

Fig. 34 shows the NFD result for the current elasto-plastic analysis under loading history $O1$. (Note that $O1$ does not include an unloading phase.) Fig. 34 suggests a trend of *softening* of the NFD curve for spheres with plastic material properties. As expected, the degree of softening increases with yield stress. These trends are in agreement with the axisymmetric investigations both in this paper and in those of other researchers (e.g., Walton, 1993; Vu-Quoc et al., 2000b; Vu-Quoc and Zhang, 1999).

Table 3
Summary of loading histories and yield stresses for elasto-plastic oblique FEA

Analysis	Loading history	σ_Y (N/m^2)	P_Y (N)
*OEP*1.1	$O1$	1.0×10^8	36.4
*OEP*1.2	$O1$	2.0×10^8	291.6
*OEP*2.1	$O2$	1.0×10^8	36.4
*OEP*2.2	$O2$	2.0×10^8	291.6

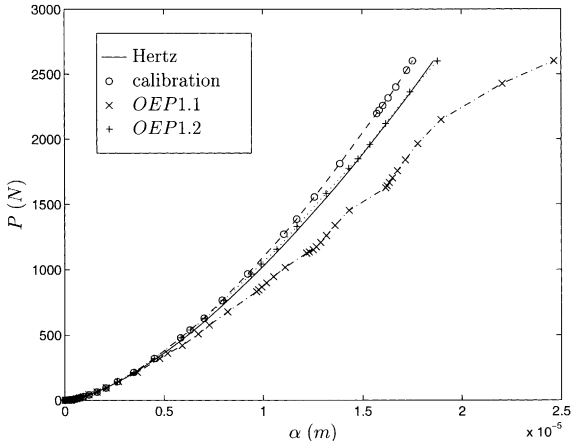

Fig. 34. Normal force P versus normal displacement α for elasto-plastic analysis under loading history $O1$.

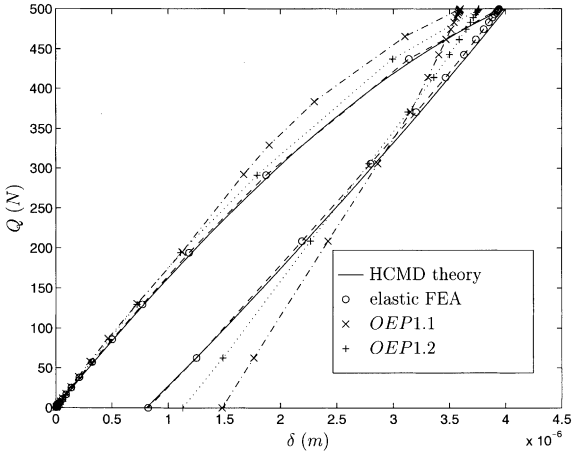

Fig. 35. Tangential force Q versus tangential displacement δ for elasto-plastic analysis under loading history $O1$.

Fig. 35 shows the TFD results for loading history $O1$. Unlike the NFD plots, the TFD results show a stiffening due to plastic flow in the sphere material. We justify the stiffening using the concept of equivalent elasticity and the HCMD theory. That is, according to Eq. (3.5), the tangential stiffness of the contact should increase when the contact-area increases. Since our normal loading analysis (together with common sense) confirms that contact-area increases with plastic flow, the increased tangential stiffness is plausible.

Fig. 36 shows the NFD results for loading history $O2$. The plot again shows softening due to the plastic flow, a behavior that is similar to that obtained for the loading history $O1$. The figure also shows the NFD behavior during unloading, where the plastic flow causes a permanent normal displacement and an energy loss within the NFD plot, (i.e., the unloading curve is different from the normal loading curve).

Fig. 37 shows the TFD result for the loading history $O2$ under the current plastic analysis. This plot shows a trend that is decidedly different from the result of the loading history $O1$. That is, while the TFD curve stiffens under constant normal force, the TFD curve appears to soften under a varying normal force. This trend poses a challenge to the development of a TFD model for particle simulation: *The model must approximate stiffening under P-constant, but it must also show softening under P-varying.*

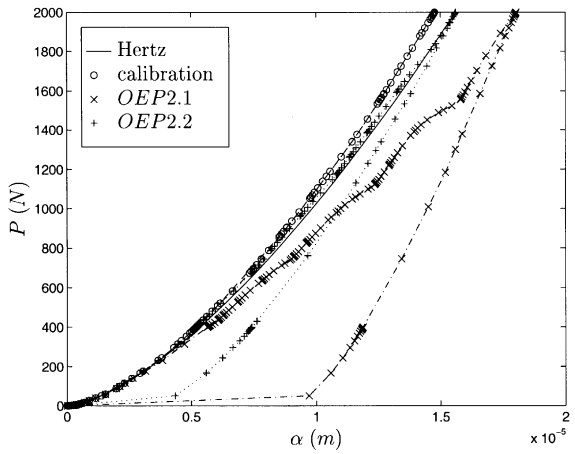

Fig. 36. Normal force P versus normal displacement α for elasto-plastic analysis under loading history $O2$.

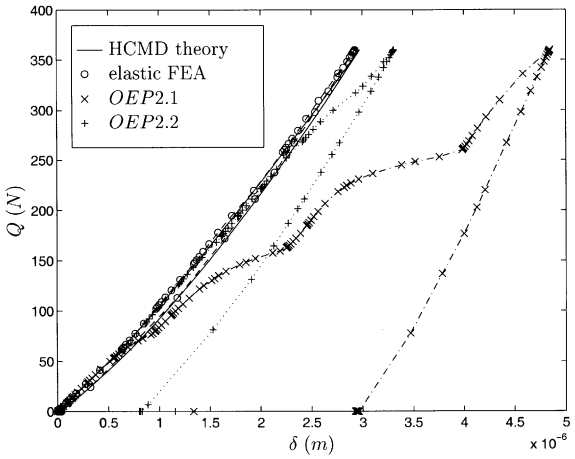

Fig. 37. Tangential force Q versus tangential displacement δ for elasto-plastic analysis under loading history $O2$.

In Fig. 37, the TFD plot for the case $OEP2.1$ (see Table 3) shows a series of severe *bumps* during most of the loading portion. During unloading, the bumps do not appear. We attribute this loading behavior to the increasing contact-area that occurs as a result of the increasing normal load. We surmise that the steep portions of the bumps correspond to new nodes being added to the contact-area. (Recall that counting additional contacting nodes is one method to measure an increase in the contact area.) The absence of bumps during unloading can be explained by the relatively slow or zero change in contact-area during that portion of the loading history. That is, permanent deformation has occurred, which corresponds to only minimal recovery of the material during unloading.

We propose that the severity of the bumps may be connected to the relative refinement of the FE mesh. As shown in Fig. 25, the contact area for the current analysis contains at most eight nodes in the radial direction. Consequently, relatively large normal force increments are required to add nodes to the contact-area. A more refined mesh (perhaps closer to the order of refinement that is shown in the axisymmetric model of Fig. 4) may decrease the normal force increment that causes increases in contact-area (or additional contacting nodes). Consequently, the FD curves may show bumps that are reduced in severity.

Table 4
Energy losses for the present oblique analyses

Case	σ_Y (N/m^2)	P_Y (N)	NFD area (Nm)	TFD area (Nm)
*OEP*1.1	1.0×10^8	36.4	N/A (no unload)	5.3722×10^{-4}
*OEP*1.2	200×10^6	291.6	N/A (no unload)	4.3246×10^{-4}
Elastic FEA, *O*1	N/A (elastic)	N/A	N/A (no unload)	3.6848×10^{-4}
HCMD theory, *O*1	N/A (elastic)	N/A	N/A (no unload)	3.7494×10^{-4}
*OEP*2.1	1.0×10^8	36.4	7.00×10^{-3}	5.63×10^{-4}
*OEP*2.2	200×10^6	291.6	2.6×10^{-3}	1.87×10^{-4}
Elastic FEA, *O*2	N/A (elastic)	N/A	4.12×10^{-5}	2.55×10^{-5}
HCMD theory, *O*2	N/A (elastic)	N/A	0	2.77×10^{-5}

Table 4 shows the energy losses that are associated with the oblique loading analyses of this section. We measure energy losses (which also correspond to different values of the coefficient of restitution in the normal loading case) via the areas within the bounds of the FD curves. These areas provide important baselines to which FD models should be compared. (Correctly representing energy loss is one of the main goals of an effective FD model.)

In summary, for the 3-D elasto-plastic FEA results, one observes an influence of the presence of the tangential force in the NFD relationship (Fig. 36) by presence of a series of *mild* bumps that correspond to the more *severe* bumps in the TFD relationship (Fig. 37). We note that there are some mild deviations from smoothness in the NFD relationship in Fig. 34, while the TFD relationship in Fig. 35 is smooth. Based on the above observation, which forms a cornerstone for our strategy in developing completely consistent elasto-plastic NFD and TFD models, we develop in Vu-Quoc et al. (2000b) and in Vu-Quoc and Zhang (1999) an elasto-plastic NFD model independent of the tangential force. Our elasto-plastic TFD model does include, however, the influence of the normal force.

Recall that we apply a friction coefficient of 0.2 throughout the oblique loading analyses. Since the tangential force never exceeds the friction limit μP, the tangential force is always less than 20% of the normal force. For cases of higher friction coefficient, the tangential force may have a significant effect on the NFD relationship.

This potential coupling between normal and tangential effects represents one of many opportunities for future analyses of elasto-plastic frictional spheres in contact. Specifically, further work is needed to fully characterize the relationships between normal and tangential stresses, and between normal and tangential FD relationships, in the presence of plasticity. In addition, further work is needed to quantify the effects of possible deviations from the assumptions of HCMD theory. For example, Cattaneo (1938a,b,c) and Mindlin (1949) both assumed that lateral frictional traction (i.e., perpendicular to the directions of the normal and tangential forces) could be neglected. Both authors also assumed a circular and planar contact-area. For spheres of elasto-plastic material, it can not be expected that these assumptions would hold true.

Analyses *OEP*1.1, *OEP*1.2, *OEP*2.1, and *OEP*2.2 required 31.0, 21.0, 56.8, and 47.5 min of CPU time. The analyses were performed on a DEC Alpha 250 workstation with 64 MB of RAM and running DEC Unix 3.2.

4. Closure

We present the data obtained from numerical experiments that are at the foundation of our successful elasto-plastic FD models in both the normal direction and tangential direction of spheres in collision. We also present in detail how these data were obtained.

Our goal is to develop elasto-plastic NFD and TFD macroscopic models that are simple and accurate in capturing the effects of plastic deformation for granular flow simulations that involve thousands or hundreds of thousands of particles. Using the observations of the elasto-plastic NFD relationship obtained from numerical experiments, we propose an efficient and accurate NFD model in Vu-Quoc et al. (2000b) (force-driven version) and in Vu-Quoc and Zhang (1999) (displacement-driven version). It is noted that the displacement-driven version is needed in granular flow simulations using discrete element method. Our elasto-plastic TFD model, which is consistent with our elasto-plastic NFD model, is presented in Vu-Quoc et al. (2000a) (force-driven version).

Acknowledgement

We thank the financial support of the National Science Foundation for this research.

References

Bitter, J.G.A., 1963. A study of erosion phenomena: part I. Wear 6, 5–21.

Brilliantov, N., Spahn, F., Hertzch, J., Pöschel, T., 1996. Model for collisions in granular gases. Physical Review E 53 (5), 5382–5392.

Cattaneo, C., 1938a. Sul contatto di due corpi elastici: distribuzione locale degli sforzi. Academia dei Lincei, Rendicotti 27 (6), 342–348.

Cattaneo, C., 1938b. Sul contatto di due corpi elastici: distribuzione locale degli sforzi. Academia dei Lincei, Rendicotti 27 (6), 434–436.

Cattaneo, C., 1938c. Sul contatto di due corpi elastici: distribuzione locale degli sforzi. Academia dei Lincei, Rendicotti 27 (6), 474–478.

Chandrasekaran, N., Haisler, W., Goforth, R., 1987. Finite element analysis of hertz contact problem with friction. Finite Elements in Analysis and Design 3, 39–56.

Cuttino, J., Dow, T., 1997. Contact between elastic bodies with an elliptic contact interface in torsion. Journal of Applied Mechanics 64, 144–148.

Davies, R., 1949. The determination of static and dynamic yield stress using a steel ball. Proceedings of the Royal Society of London Series A A197, 416–432.

Goldsmith, W., 1960. Impact: The Theory and Physical Behaviour of Colliding Solids. Edward Arnold, London.

Hardy, C., Baronet, C., Tordion, G., 1971. The elasto-plastic indentation of a half-space by a rigid sphere. International Journal for Numerical Methods in Engineering 3, 451–462.

Hertz, H., 1882. Über die Berührung fester elastischer Körper (on the contact of elastic solids). J. Reine und Angewandte Mathematik 92, 156–171.

ABAQUS/Standard User's Volume 1, version 5.5, Hibbitt, Karlsson, and Sorensen, Pawtucket, RI, 1995.

Jaeger, J., 1992. Elastic impact with friction. Ph. D. Thesis, Delft University, Netherlands.

Jaeger, J., 1999. A generalization of Cattaneo–Mindlin for thin strips. ASME Journal of Applied Mechanics 66, 1034–1037.

Johnson, K.L., 1985. Contact Mechanics. 2nd Edition, Cambridge University Press, New York.

Kral, E.R., Komvopoulos, K., Bogy, D.B., 1993. Elastic–plastic finite element analysis of repeated indentation of a half-space by a rigid sphere. ASME Journal of Applied Mechanics 60, 829–841.

Kral, E.R., Komvopoulos, K., Bogy, D.B., 1995a. Finite element analysis of repeated indentation of an elastic–plastic layered medium by a rigid sphere. Part I: surface results. ASME Journal of Applied Mechanics 62, 20–28.

Kral, E.R., Komvopoulos, K., Bogy, D.B., 1995b. Finite element analysis of repeated indentation of an elastic–plastic layered medium by a rigid sphere. Part II: subsurface results.. ASME Journal of Applied Mechanics 62, 29–42.

Mindlin, R.D., 1949. Compliance of elastic bodies in contact. ASME Journal of Applied Mechanics 16, 259–268.

Mindlin, R.D., Deresiewicz, H., 1953. Elastic spheres in contact under varying oblique forces. ASME Journal of Applied Mechanics 20, 327–344.

Mishra, B.K., 1995. Ball charge dynamics in a planetary mill. KONA Powder and Particle 13, 151–158.

Shih, C.W., Schlein, W.S., Li, J.C.M., 1992. Photoelastic and finite element analysis of different size spheres in contact. Journal of Materials Research 7 (4), 1011–1017.

Sinclair, G., Follansbee, P., Johnson, K., 1985. Quasi-static normal indentation of an elasto-plastic half-space by a rigid sphere, II: results. International Journal of Solids and Structures 21 (8), 865–888.

Thornton, C., 1997. Coefficient of restitution for collinear collisions of elastic perfectly plastic spheres. ASME Journal of Applied Mechanics 64, 383–386.

Thornton, C., Randall C.W., 1988. Applications of theoretical contact mechanics to solid particle system simulation. in: M. Satake, J.T. Jenkins (Eds.), Micromechanics of Granular Materials, Elsevier, Amsterdam, pp. 133–142.

Vu-Quoc, L., Zhang, X., 1999. An elastoplastic contact force–displacement model in the normal direction: displacement-driven version. Proceedings of the Royal Society of London, Series A 455, 4013–4044.

Vu-Quoc, L., Lesburg, L., Zhang, X., 2000a. A tangential force–displacement model for contacting spheres accounting for plastic deformation: force-driven formulation. Journal of the Mechanics and Physics of Solids, submitted for publication.

Vu-Quoc, L., Zhang, X., Lesburg, L., 2000b. A normal force–displacement model for contacting spheres accounting for plastic deformation: force-driven formulation. ASME Journal of Applied Mechanics 67 (2), 237–436.

Vu-Quoc, L., Zhang, X., Walton, O.R., 2000c. A 3-D discrete element method for dry granular flows of ellipsoidal particles. Computer Methods in Applied Mechanics and Engineering Invited paper for the special issue on Dynamics of Contact/Impact Problems 187(3–4), 483–528.

Walton, O.R., 1993. Numerical simulation of inelastic, frictional particle–particle interactions. In: Roco M.C. (Ed.), Particulate Two-Phase Flow. Butterworth-Heinemann, Stoneham, MA, pp. 884–911 (Chapter 25).